# Energy Transport and Conversion Within Earth's Supercritical Bow Shock: The Role of Intense Lower-Hybrid Whistler Waves

Arthur J Hull, Laurent Muschietti, Oleksiy V Agapitov, Christopher C Chaston, Olivier Le Contel, Per-arne Lindqvist

JGR Space Physics

RESEARCH ARTICLE
10.1029/2023JA031630

# Energy Transport and Conversion Within Earth's Supercritical Bow Shock: The Role of Intense Lower-Hybrid Whistler Waves

**Arthur J. Hull[1], Laurent Muschietti[1,2], Oleksiy V. Agapitov[1], Christopher C. Chaston[1], Olivier Le Contel[3], and Per-Arne Lindqvist[4]**

[1]Space Sciences Laboratory, University of California, Berkeley, CA, USA, [2]LATMOS-IPSL-UVSQ-CNRS, Guyancourt, France, [3]Laboratoire de Physique des Plasmas, UMR7648, CNRS, Sorbonne Université, Université Paris-Saclay, Observatoire de Paris, Ecole Polytechnique Institut Polytechnique de Paris, Paris, France, [4]Royal Institute of Technology, Stockholm, Sweden

**Key Points:**

- Whistler waves near lower-hybrid frequencies play an integral role in the reconfiguration of energy at high Mach number collisionless shocks
- Whistler mediated energy transport and exchange depends on scale and location within the layer
- Whistlers transport energy along the shock and slightly toward the ramp where it gets dissipated into electron heating via Landau damping

**Correspondence to:**
A. J. Hull,
ahull@berkeley.edu

**Citation:**
Hull, A. J., Muschietti, L., Agapitov, O. V., Chaston, C. C., Le Contel, O., & Lindqvist, P.-A. (2024). Energy transport and conversion within Earth's supercritical bow shock: The role of intense lower-hybrid whistler waves. *Journal of Geophysical Research: Space Physics*, *129*, e2023JA031630. https://doi.org/10.1029/2023JA031630

Received 21 APR 2023
Accepted 28 MAR 2024



**Abstract** Detailed analysis of a high Mach number quasiperpendicular Earth bow shock crossing by the Magnetospheric Multiscale (MMS) spacecraft fleet reveal that lower-hybrid (LH) whistler waves generated in the shock foot region transport energy predominately along the shock surface and slightly toward the shock ramp in the shock normal incidence frame, where wave energy accumulates and is dissipated into the plasma. This suggests the LH whistlers play an integral role in energy reconfiguration at high Mach number collisionless shocks with ramifications to plasma heating. The multipoint observations are used to quantify the wave characteristic parameters (via interferometry), Poynting fluxes, and energy conversion rates $D$, and to assess their scale dependencies and spatial and temporal properties. The whistler associated energy transport and conversion are found to depend on scale and location within the layer. High-frequency electrostatic waves yield largest values of $D$. However, the dominant net energy exchange contribution is from the LH whistlers. In the foot spatially temporally coherent net energy exchange from the plasma to whistlers is observed, whereas deeper in the ramp net wave energy dissipation to the plasma is observed exhibiting significant space-time variability. These results are consistent with the modified two stream instability driven by the relative drift between reflected ions and electrons as the mechanism for wave growth in the foot. Owing to strong electron heating, whistler energy dissipation in the ramp is attributed to Landau damping, which out-competes the destabilizing effect of the reflected ion and electron drift.

## 1. Introduction

Studies indicate that whistler waves at lower-hybrid (LH) frequencies and below play an essential role within high-Mach number supercritical fast mode shock layers (e.g., Bale et al., 2005; Balikhin et al., 1997; Dimmock et al., 2013; Hull et al., 2012; Hull et al., 2020; Krasnosel'skikh et al., 1991; Krasnoselskikh et al., 2013; Sundkvist et al., 2012; Wilson et al., 2014a, Wilson et al., 2014a, Wilson, 2016). Under high-Mach number conditions, such low-frequency (LF) whistlers, being much more intense, are associated with large amplitude magnetic fields ($\delta B/B_0 \sim 0.1-1.0$) and sizable currents that significantly affect shock internal structure and thus can have significant ramifications to shock energy transport and dissipation processes. The intense whistler magnetic fields add sizable short spatial scale nonmonotonic variations within the shock foot and ramp that can induce perpendicular anisotropies in electron distributions that lead to secondary high-frequency (HF) whistler waves ($f \sim 0.1$–$0.5\, f_{ce}$, with $f_{ce}$ being the electron cyclotron frequency) (Hull et al., 2012, 2020). Additionally, the current densities the LF whistlers carry dominate the shock macroscale current densities (by factors up to 40–50), providing a free energy source for other wave modes, such as large amplitude electrostatic (ES) waves, which also modify the shock structure and can influence plasma transport (e.g., Hull et al., 2020; Wilson et al., 2014a; Wilson et al., 2014b). With the currents and electric fields they carry, the whistlers can transfer their energy to the plasma and vice versa (Hull et al., 2020; Wilson et al., 2014a, 2014b). The recent study by Hull et al. (2020) of a high Mach number quasiperpendicular shock crossing by the MMS mission revealed that whistler-associated energy exchange depends on location within the layer, with conversion of plasma energy to wave energy found to occur in the foot while exhibiting dissipation of wave energy into the plasma in the ramp. They suggested that these results indicate that whistler waves generated in the foot are carried to the ramp where they are dissipated into plasma energization. However, Hull et al. (2020) did not report wave Poynting fluxes to confirm this notion. Whistlers near the LH frequency were observed to have upstream directed Poynting fluxes in the rest frame of two high-Mach

number quasiperpendicular shocks in the study by Sundkvist et al. (2012). They suggested that the whistlers play a role in energy repartitioning, with energy being dissipated through wave-particle interactions, presumably upstream of the shock front, seemingly in contradiction with the conclusions of Hull et al. (2020). Note, energy exchange rates $D = \mathbf{J} \cdot \mathbf{E}$ (with $\mathbf{J}$ and $\mathbf{E}$ being the current density and electric field) were not quantified in Sundkvist et al. (2012) and it is unknown whether the properties are similar or differ from those reported by Hull et al. (2020). Though significant progress has been made, more work is needed to better understand the role whistler waves play in the relationship between energy transport and conversion processes, and their dependency on scales as a function of location within the layers of high Mach number quasiperpendicular shocks.

In this study, we revisit the Earth bow shock event reported in the study by Hull et al. (2020). This study is complementary in that we further assess the properties of the whistler waves, and examine the nature of Poynting fluxes these waves carry and their relation to energy exchange/dissipation within the layer, including their dependencies on scale and spatial-temporal properties. Whistler waves at shocks occur in the frequency range between the ion cyclotron frequency and the electron cyclotron frequency ($f_{ci} < f < f_{ce}$). In this study, attention is primarily focused on LF whistler waves that occur at spacecraft frame frequencies near and below the LH frequency. To dynamically characterize the properties of the LF whistler waves, we utilize interferometry (Labelle & Kintner, 1989). Our approach differs from that used by Dimmock et al. (2013), who employed dual spacecraft interferometry combined with minimum variance analysis to determine phase velocities, wave vectors, and hence the dispersion relation of LF whistler waves upstream of a quasiperpendicular shock. Here, we applied a wavelet-based interferometry method to measurements from all four MMS spacecraft. This approach is enabled by the long-duration, high-time resolution fields sampled on four closely spaced (~11–18 km) spacecraft. In addition to providing accurate determinations of phase velocities and rest frame frequencies, this approach also yields accurate estimates of wavelengths/scales of the waves. Using this information, we quantify, for the first time, the scale dependency of the Poynting fluxes and energy conversion rates over the frequencies spanning the LF whistler fluctuations. These results provide novel insight into the energy transport and exchange processes associated with these waves within the shock layer.

## 2. Instrumentation, Experimental Data Set, and Methodology

This study used magnetic field observations from the MMS fluxgate magnetometer (FGM) and search-coil magnetometer (SCM) instruments (Le Contel et al., 2016; Russell et al., 2016). These instruments provide magnetic field measurements at a rate of 128 and 8,192 S/s, respectively. We also used electric field measurements sampled at a rate of 8,192 S/s from the axial and spin plane double-probe electric field instruments (ADP and SPD) on MMS (Ergun et al., 2016; Lindqvist et al., 2016). In addition, we used electron and ion measurements sampled at rates of ~33 and ~6.7 S/s from the fast plasma investigation (FPI) on MMS (Pollock et al., 2016).

To characterize the waves and determine the scale dependency of associated Poynting fluxes and energy conversion rates, we used interferometry (e.g., Labelle & Kintner, 1989). With this method, the wave vectors and phase velocities are spectrally determined and hence we obtain the wavelengths/spatial scales. To quantify these parameters, a Morlet wavelet-based cross-spectral analysis technique (Eriksson, 1998; Torrence & Compo, 1998; Torrence & Webster, 1999) is employed to determine the coherency $R^{\nu 2}_{\alpha\beta}(t)$ and phase difference ($\phi^{\nu}_{\alpha\beta}(t)$, with $\alpha \neq \beta = 1 - 4$) of magnetic field fluctuations as a function of frequency $f_\nu$ and time between all possible spacecraft pairs (six unique pairs for MMS). Here, we used the Torrence and Webster (1999) formulation for wavelet coherence at a given frequency and time defined as:

$$R^{\nu 2}_{\alpha\beta}(t) = \frac{|<\Psi^{\alpha\beta}_{\nu}(t)>|^2}{<|\Psi^{\alpha}_{\nu}(t)|^2><|\Psi_{\nu}(t)^{\beta}|^2>}, \quad (1)$$

where the wavelet cross-spectral density is given by $\Psi^{\alpha\beta}_{\nu}(t) = \Psi^{\alpha}_{\nu}(t)\Psi^{\beta *}_{\nu}(t)$ with $\Psi^{\alpha}_{\nu}$ and $\Psi^{\beta}_{\nu}$ denoting the Morlet wavelet transform of time series of one magnetic field component measured by the $\alpha$ and $\beta$ spacecraft pair. The symbol * denotes the complex conjugate and the brackets $< >$ represent an average over time and wavelet scale $s_\nu$. Note, the scale $s_\nu$ is related to Fourier frequency by the expression $f_\nu^{-1} = 4\pi s_\nu / \left(\omega_0 + \sqrt{2 + \omega_0^2}\right) \approx s_\nu$ (Torrence & Compo, 1998), with the non-dimensional frequency being set to $\omega_0 = 2\pi$ by design (Eriksson, 1998).

The phase difference is given by the relation:

$$\phi^{\nu}_{\alpha\beta}(t) = \tan^{-1}\frac{\mathcal{I}\{<\Psi^{\alpha\beta}_{\nu}(t)>\}}{\mathcal{R}\{<\Psi^{\alpha\beta}_{\nu}(t)>\}}, \tag{2}$$

where $\mathcal{I}$ and $\mathcal{R}$ denote the imaginary and real parts, respectively. Given the phase differences, the wave unit vectors and phase velocities are determined using a four spacecraft least squares method (Harvey, 1998). This method, which depends on the relative spacecraft positions and signal time delays, is based on minimizing the function:

$$\mathcal{F}_{\nu} = \sum_{\alpha=1}^{4}\sum_{\beta=1}^{4}\left[\hat{\mathbf{k}}^{\nu}\cdot(\mathbf{r}_{\alpha}-\mathbf{r}_{\beta}) - V_{\nu}t^{\nu}_{\alpha\beta}\right]^2, \tag{3}$$

where $\hat{\mathbf{k}}^{\nu}$ and $V_{\nu}$ are the wave unit vector and phase velocity of sufficiently coherent waves at a given frequency $f_{\nu}$, $t^{\nu}_{\alpha\beta} = t^{\nu}_{\alpha} - t^{\nu}_{\beta} = \phi^{\nu}_{\alpha\beta}/(2\pi f_{\nu})$ is the time delay of the signal at frequency $f_{\nu}$ between the $\alpha$ and $\beta$ spacecraft, and $\mathbf{r}_{\alpha,\beta}$ is the position vector of the $\alpha$, $\beta$ spacecraft. Minimization of Equation 3 for a given frequency $f_{\nu}$ and time yields the following expression:

$$m^{\nu}_{l} = \frac{1}{32}\left[\sum_{\alpha=1}^{4}\sum_{\beta=1}^{4} t^{\nu}_{\alpha\beta}(r_{\alpha k} - r_{\beta k})\right] R^{-1}_{kl}, \tag{4}$$

where $m^{\nu}_{l}$ is the $l$th component of vector $\mathbf{m}^{\nu} \equiv \hat{\mathbf{k}}^{\nu}/V_{\nu}$ and $R^{-1}_{kl}$ is the inverse of the volumetric tensor given by:

$$R_{kl} = \frac{1}{4}\sum_{\alpha=1}^{4} r_{\alpha k} r_{\alpha l}. \tag{5}$$

The wave unit vector is thus given by $\hat{\mathbf{k}}^{\nu} = \mathbf{m}^{\nu}/|\mathbf{m}^{\nu}|$ and the phase velocity is $V_{\nu} = 1/|\mathbf{m}^{\nu}|$. For additional details on how these expressions are derived, we refer the reader to Section 12.2.2 of Harvey (1998).

The wavelet-based approach used here is a natural extension of the method described by Harvey (1998) to spectrally decomposed field components, enabling a global determination of the properties of the waves. The Morlet wavelet transform is used because it more accurately resolves the intermittent behavior of the wave fields with spacecraft frame frequency. This method provides high-quality estimates of $\hat{\mathbf{k}}^{\nu}$ and $V_{\nu}$ provided that the wavelet decomposed signals are sufficiently similar on all four spacecraft and the delay times are well resolved from the sampling period $T_s$. The quality of the estimates of $\hat{\mathbf{k}}^{\nu}$ and $V_{\nu}$ is evaluated ex post facto using two criteria. One criterion used is the requirement that the delay times on at least five baselines satisfy the conditional $t_{\alpha\beta} \geq 3T_{\mathrm{Nyq}} = 6T_s$, where $T_{\mathrm{Nyq}} = 2T_s$ is the Nyquist period. From experience in comparing wave vectors determined via the Harvey method and minimum variance applied to pass-filtered time domain data (e.g., Hull et al., 2020), this requirement is a necessary, but not sufficient, constraint in discriminating good determinations from unresolved timings that can produce unphysical results. A valid result is obtainable even when the delay time approaches the Nyquist limit on one baseline (tantamount to being nearly perpendicular to the baseline), owing to the fact that the MMS tetrahedron is not degenerate (e.g., the spacecraft do not lie in a plane) and has similar baseline lengths in the region of interest. For signals at frequencies $\lesssim$ tens of Hz sampled in SCM burst data, $t_{\alpha\beta} \sim$ tens to hundreds of $T_s$ are usually obtained on at least five baselines. In addition, a coherency threshold of 0.5 is imposed for all baseline pairs to ensure that the signals are sufficiently "similar". These combined criteria effectively alleviate issues from weak or uncorrelated signals and multiple modes in a given bin. Given $V_{\nu}$, the characteristic wavelengths are just $\lambda_{\nu} = V_{\nu}/f_{\nu}$, which can be used to transform quantities from frequency space to wavelength (or wave number) space. Note, $V_{\nu}$ and $f_{\nu}$ are defined with respect to the spacecraft frame. The phase speed in the plasma rest frame is obtained from the expression $V_{o\nu} = V_{\nu} - \mathbf{U}_{\mathrm{cm}}\cdot\hat{\mathbf{k}}^{\nu}$, where $\mathbf{U}_{\mathrm{cm}}$ is the center of mass bulk velocity. Similarly, the rest frame frequency is obtainable from $f_{o\nu} = f_{\nu} - \mathbf{U}_{\mathrm{cm}}\cdot\hat{\mathbf{k}}^{\nu}/\lambda_{\nu}$.

## 3. Observations

The shock event of interest is an inbound crossing (upstream to downstream) of Earth's bow shock at 0805 UT on 04 November 2015 by MMS. This shock was featured in the recent study by Hull et al. (2020), who showed that the electromagnetic fluctuations from a few Hz and above within the foot and ramp have characteristics of whistler waves. However, they did not address the spatial-temporal nature of Poynting fluxes and energy conversion rates, nor dependencies on scale. The shock is quasiperpendicular, with the angle between the shock normal and upstream asymptotic magnetic field determined to be $\theta_{bn1} = 82° \pm 2°$. The normal is given by $\hat{\mathbf{n}} = [0.9867, 0.1615, -0.01916]$ in GSE coordinates and the upstream magnetic field vector is $\mathbf{B_1} = [-2.195, 7.194, -1.482]$. The event occurred under high solar wind flow and dynamic pressure conditions, with the upstream velocity along the normal in the shock rest frame being $U_n \sim 735$ km/s and dynamic solar wind pressure $P_{\rm SW} \sim 7$ nPa, respectively. The upstream fast mode and Alfvén Mach numbers are high, with values estimated at $M_f \sim 6.7$ and $M_A \sim 10$, respectively. For additional details on the shock characteristic parameters and their determination, we refer the reader to the paper by Hull et al. (2020).

### 3.1. Wave Characteristics Based on Interferometry

In this study, we dynamically assessed the properties of the LF whistler waves in the shock using interferometry based on the Morlet wavelet cross-spectral analysis discussed above in Section 2. The interferometric results for this shock crossing are shown in Figure 1. For context, Figure 1a shows an overview of the magnetic field magnitude spanning the upstream to downstream side of the shock. The field was boxcar averaged using a 12 s window to reveal the shock macroscale structure. Figures 1b–1d display the magnetic field amplitude, normalized magnetic field (from merged FGM and SCM data) power spectral densities (PSDs), and magnetic field polarization from MMS1 in the zoomed in region of the foot and ramp, respectively. The magnetic field PSDs were dynamically determined from time series data using a Morlet wavelet transformation. The Morlet wavelet is an ideal choice because the PSDs with proper normalization are comparable to Fourier-derived PSDs (Eriksson, 1998). To make apparent structure at higher frequencies, the PSDs were rescaled by multiplying them by frequency. Within a constant factor, the rescaled PSDs denote the relative contribution to the total integrated power. Namely, $P^{\rm total}(t) = \Delta x \sum[\text{PSD}\,(f, t)f]$, where $\Delta x = \Delta f/f$ is a constant by design. The normalized magnetic field PSDs reveal the presence of broad frequency band electromagnetic fluctuations spanning from a fraction of a Hz up to a few 10–100s of Hz depending on location in the interval. Bursts of activity appear to be collocated with gross enhancements in the magnetic field substructure (green curve) in Figure 1b. The most intense contributions to power at any given location are from fluctuations near and below the LH frequency, which is indicated by the middle white curve in Figures 1c–1j. These LF waves were identified as whistler waves in the study by Hull et al. (2020) using a combination of timing and hodogram analysis applied to some examples of finite pass-band-filtered waveforms. The LF whistlers exhibit right-hand polarized magnetic signatures (red), which are most apparent near the beginning of the interval to 0805:50 UT in Figure 1d. After this, the polarization becomes less discernible, which appears to be associated with mixed modes within a given frequency bin. Though not the focus of this study, HF whistler waves are also observed and manifested as the right-hand polarization signatures at a few 100 Hz frequencies. According to Hull et al. (2020), the HF whistlers arise from preferential perpendicular anisotropies induced in electron distributions via their interaction with the intense non-monotonic magnetic fields of the LF whistlers.

To dynamically determine the properties of the LF whistlers in the interval, cross-spectral analysis was applied to all possible spacecraft pairs of the magnetic field vector x component in GSE coordinates to determine the phase differences between coherent fluctuations. This information is subsequently used to determine the wave vectors, phase velocities, and scales. Figure 1e shows the wavelet coherencies (Torrence & Webster, 1999) as a function of frequency and time of signals measured by the MMS1 and MMS3 spacecraft determined from Equation 1. The results indicate that magnetic fluctuations observed by the two spacecraft at frequencies up to several tens of Hz in the first half and up to ∼10 Hz in the second half of the layer generally covary and thus have well-defined/consistent phase relationship in the interval (i.e., coherencies ≥0.6 indicated in yellow to red in Figure 1e). This range of frequencies encompasses quite well the LF whistlers that are the focus of this paper. With some exceptions, the coherencies at higher frequencies vary significantly at reduced levels (<0.5), indicating that the magnetic fluctuations at these frequencies are generally incoherent, as they exhibit space-time variability within the short spacecraft separations. Similar coherency results were obtained from the other baseline comparisons (not shown).

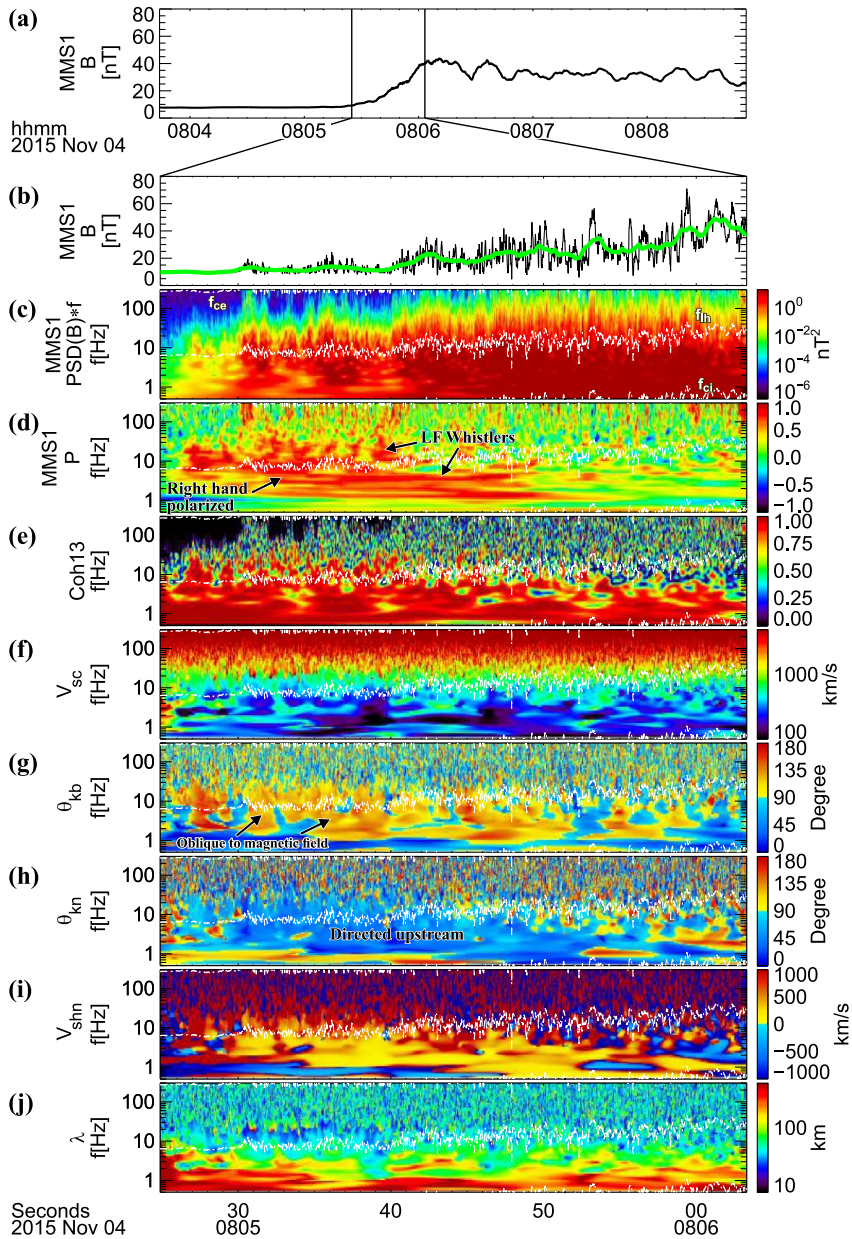


**Figure 1.** (a) Overview of magnetic field amplitude from MMS1. In zoomed in interval are shown the (b) magnetic field amplitude sampled at 128 S/s (black) and 1s boxcar averaged (green), (c) magnetic field power spectral densities, and (d) polarization spectra from MMS1, (e) coherency between magnetic fields measured by MMS1 and MMS3, (f) phase velocities in the spacecraft frame, (g) angle between the wave unit vector $\hat{\mathbf{k}}$ and magnetic field, (h) angle between $\hat{\mathbf{k}}$ and shock normal $\hat{\mathbf{n}}$, (i) phase velocities in shock frame along the upstream directed shock normal, and (j) wavelengths. Red (blue) in (d) corresponds to right-hand (left-hand) polarized waves. The white curves in (c)–(j) indicate the ion cyclotron ($f_{ci}$), lower-hybrid ($f_{lh}$), and electron cyclotron ($f_{ce}$) frequencies, respectively.

The phase velocities in the spacecraft frame $V_{SC}$ determined by the Harvey (1998) method are shown in Figure 1f. Using the coherencies above 0.5 as a guide, the spacecraft frame phase velocities associated with coherent LF whistlers are found to increase with increasing frequency, with values ranging from ∼100 km/s at a few Hz to ∼1,000 km/s at a few 10s of Hz, which yield a median of 320 km/s over the full interval. Figure 1g shows the angle between the wave vector and the background magnetic field $\theta_{kb}$. Note, whistler waves can impact the direction of the background magnetic field. Thus, for spectral quantities organized by the field in this paper (e.g., $\theta_{kb}$ or polarization), the background magnetic field (based on merged FGM and SCM data) is frequency

dependent and is determined for each frequency $f$ via boxcar smoothing of time series data using a $10/f$ window. Though there are some exceptions, the LF whistler wave vectors are preferentially oriented at oblique angles with respect to the background magnetic field with values for $\theta_{kb}$ generally ranging from ~110°–135° with a peak value at 123°. Figure 1h demonstrates that the LF whistler wave vectors projected along the normal are generally directed upstream at angles ranging from $\theta_{kn}$ ~30°–80°, with a median of 52° in the interval. The wave vectors have a slight preferential inclination toward the magnetic coplanarity plane (plane containing the shock normal and asymptotic magnetic field), with peak and median angles found to be 35° and 41°, respectively (not shown). The phase velocities along the normal in the shock rest frame are generally upstream directed, with values ranging from ~200 to ~1,400 km/s with a median of ~500 km/s (see Figure 1i). Interestingly, an exception occurs at spacecraft frame frequencies $\lesssim$ 1 Hz, where the whistlers are more quasiparallel to the magnetic field. These whistlers are shown to have phase velocities that are directed downstream toward the shock ramp. Figure 1j depicts wavelengths, which for the LF whistler waves, range from a few tens of km at spacecraft frame frequencies of a few tens of Hz to nearly 1,000 km at a few Hz, with a median value of $\lambda = 120$ km. Normalized to the ion inertial length this range of scales spans $\lambda/\lambda_i$ ~0.3–8, respectively, with a median of $\lambda/\lambda_i$ ~2. The rest frame frequencies of the LF whistler waves range from $f_\circ$ ~$0.7 - 40$ Hz, with a mean of 5.2 Hz. These values correspond to normalized frequencies $f_\circ/f_{\rm lh}$ of 0.04–6.3 with a mean of 0.5, and $f_\circ/f_{\rm ci}$ of 1.7–270 with a mean of 21. This demonstrates that the LF whistlers are predominantly in the LH whistler regime. These results are consistent with and dramatically extend the results of Hull et al. (2020).

### 3.2. Energy Conversion Rates

Hull et al. (2020) examined energy conversion rates in the shock normal incidence frame (NIF) associated with whistler waves at and below 30 Hz from one MMS spacecraft. The results indicated that energy was being exchanged from the plasma to wave energy in the foot, while dissipation of wave energy to the plasma occurred in the second half of the foot/ramp region. Here, we extend the frequency range from $f < 30$ Hz (Hull et al., 2020, case) to $f < 4$ kHz to assess low and high frequency contributions to conversion rates in the plasma rest frame defined as $D_\circ = \mathbf{J}\cdot\mathbf{E}_\circ$. The $\mathbf{E}_\circ$ is the plasma frame electric field determined from spacecraft frame measurements using the relation $\mathbf{E}_\circ = \mathbf{E}_{\rm SC} + \mathbf{U}_{\rm cm} \times \mathbf{B}$, where $\mathbf{U}_{\rm cm}$ is the center of mass bulk velocity. We also explore the spatial-temporal variability of $D_\circ$ based on measurements taken at the four individual spacecraft. Figure 2 shows quantified conversion rates in the plasma rest frame for the same interval shown in Figure 6 of Hull et al. (2020). This interval covers the foot and ramp region up to the magnetic overshoot (see Figure 2a).

Figure 2d shows $\mathbf{E}_{\circ 1}$ in GSE coordinates observed by MMS1, which exhibits spiky signatures with large amplitudes reaching over 100 mV/m in the layer. These spiky electric fields are due to electrostatic (ES) waves, which appear as the broadband signatures at frequencies near and above 100 Hz in the dynamic normalized PSDs of $\mathbf{E}_{\circ 1}$ shown in Figure 2c. These high-frequency (HF) ES waves have no magnetic field counterpart in the normalized magnetic field PSDs shown in Figure 2b. Also apparent in Figure 2c are whistler associated electric fields, which are the signatures at frequencies up to tens to few hundred Hz depending on location that covary with their magnetic field PSD counterparts in Figure 2b. Figure 2e shows the current density magnitudes $\rm J_{mom1}$ and $\rm J_{mom4}$ from MMS1 (red) and MMS4 (black) determined from electron and ion moments. Current densities in the foot peak at 0.5–1 $\mu A/m^2$, while deeper in the layer values range from 1 to 3 $\mu A/m^2$, with some instances reaching 4–6 $\mu A/m^2$. Multipoint comparisons indicate that the current densities agree quite well in the foot showing little differences among the two spacecraft. Deeper in the layer, notable differences are often observed indicating space-time variability.

Figures 2f and 2g show values for $D_\circ$ from all four spacecraft at frequencies $f < 4$ kHz and $f < 30$ Hz, respectively. The values for $D_\circ$ for a given spacecraft were determined from currents estimated from moments and $\mathbf{E}_\circ$ low-pass-filtered at 30 Hz and the ~4 kHz Nyquist limit, respectively. The current densities were interpolated to the electric field time tags prior to computing $D_\circ$. The multipoint comparisons in Figures 2f and 2g reveal that the $D_\circ$ in the two frequency ranges are bursty and patchy in nature, with significant spatial and temporal variations within the interval. The amplitudes increase with increasing penetration into the shock layer, due to the intensification of the electric fields and currents. The values for $D_\circ$ determined over the full frequency range ($f < 4$ kHz) are dramatically higher by factors of 10–100 than those for frequencies $f < 30$ Hz. This is because the quantities at $f < 30$ Hz generally contain the effects of relatively low-frequency whistlers, whereas those at $f < 4$ kHz also include the effects of the large amplitude HF ES waves (see Figures 2c and 2d). Also, Figure 2g shows that the energy conversion rates have a negative bias in the first half of the interval but transition to a more

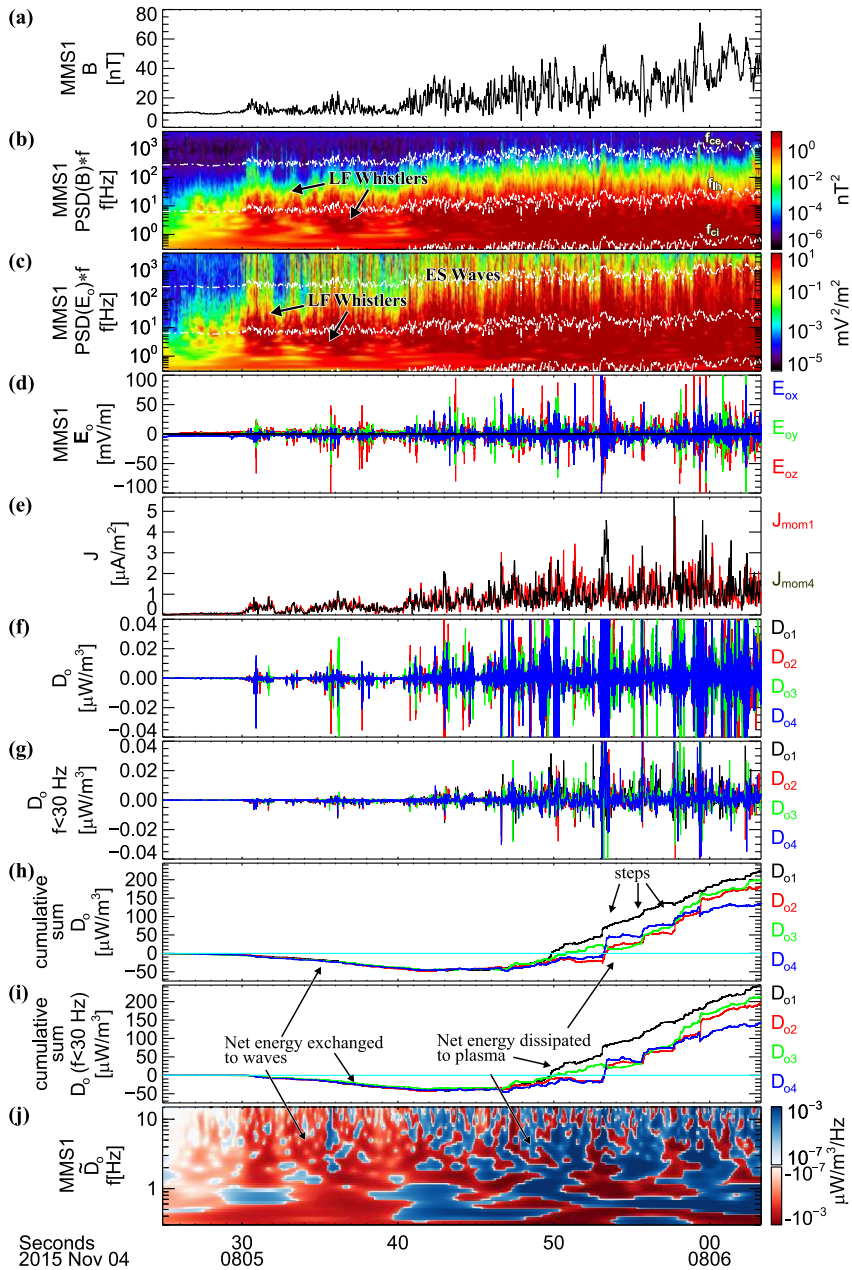


**Figure 2.** (a) Magnetic field amplitude, normalized power spectral densities of the (b) magnetic field and (c) plasma frame electric field, (d) electric field vector in plasma frame, (e) magnitude of current densities from MMS1 and MMS4, energy conversion rates in the plasma rest frame $D_o$ at frequencies (f) $f < 4$ kHz and (g) $f < 30$ Hz from all four spacecraft, the cumulative sum of $D_o$ for fields at (h) $f < 4$ kHz and (i) $f < 30$ Hz, and (j) energy conversion rate dynamic spectra $\tilde{D}_{o1}$ from MMS1. The white curves in (b) and (c) indicate the ion cyclotron ($f_{ci}$), lower-hybrid ($f_{lh}$), and electron cyclotron ($f_{ce}$) frequencies, respectively.

or less positive bias in the second half. Note, negative values for $D_o$ indicate energy extraction from the plasma to the waves, while positive values indicate wave energy dissipation to the plasma. This behavior is unclear in Figure 2f, which exhibits relatively more balanced oscillations.

To examine the spatial and temporal behavior of the net amount of energy exchanged per unit volume per unit time, Figures 2h and 2i display the cumulative sum of $D_o$ for all four spacecraft at $f < 4$ kHz and $f < 30$ Hz, respectively. Note, the cumulative sum is the running total of a time sequence of a given quantity. Given a time sequence of conversion rates for a specific spacecraft in array form [$D_{o1}$, $D_{o2}$, $D_{o3}$, …], the cumulative sum is

just [$D_{\circ t1}$, $D_{\circ t1} + D_{\circ t2}$, $D_{\circ t1} + D_{\circ t2} + D_{\circ t3}$,…]. Though there are some differences, comparisons reveal that the cumulative sums of $D_\circ$ in the two frequency ranges have the same basic shape. Namely, the sums in the two ranges decrease by similar amounts in the first half of the interval, while the sums increase by similar amounts in the second half with increasing penetration into the ramp region just before the shock overshoot region. The similar shapes indicate that the dominant net energy exchange contributions are between the LF waves ($f < 30$ Hz) and the plasma, with the HF ES waves providing negligible/net zero total contribution from individual packets in the interval. This latter behavior is likely owing to the symmetric oscillatory nature of the HF ES waves about the mean field in the interval. Additionally, the net decrease in the cumulative sums in the first half of the interval indicates a net energy exchange from the plasma to the waves. The cumulative sums in this interval show little differences from spacecraft to spacecraft, suggesting that the LF whistler wave production here is reasonably coherent. Consistent with this result, the wave magnetic field coherencies from all spacecraft pairs are generally $\gtrsim$0.6 at frequencies extending to tens of Hz in this interval (as exemplified in Figure 1e). This interpretation is further supported by the close agreement in the current densities from multiple spacecraft (Figure 2e) and the dominant, well-defined, right-hand polarization signatures (Figure 1d) exhibited in this region. The net increase in the cumulative sums in the second half of the interval demonstrates that a net amount of LF wave energy gets dissipated into the plasma there. In contrast to the first half results, departures of up to 40%–50% in the net energy dissipation into the plasma is observed among spacecraft comparisons. The differences are indicative of spatial and temporal variations in the waves within the short spatial separations of the MMS spacecraft in that region. This is signified by the reduced coherencies (<0.5) of waves near and above 10 Hz frequencies in that region mentioned above in Section 3.1. The departures arise from changes in the rate of energy accumulation (i.e., changing slopes) among the spacecraft. There are some instances within the second half of the interval where sudden localized (∼0.1–0.15 s) increases or decreases interrupt the gross increase in the cumulative sums. Examination of Figure 2a reveals that the localized steps coincide with sharp enhancements in the magnetic field. Figure 2d shows that these are associated with enhanced current densities that exhibit significant spatial and/or temporal differences among MMS spacecraft measurements. Detailed inspection of electric and magnetic field power spectra, polarization, and pass-filtered waveform observations (not shown) in the vicinity of the steps indicate that these steps appear to be due to the superposed effects of enhanced broadband whistler activity at frequencies spanning from roughly 5–10 Hz to 20–30 Hz depending on location. These intense whistlers are associated with large amplitude electric fields reaching roughly 30–70 mV/m over the frequencies spanned by these waves (not shown), with one example reaching 100 mV/m (first step on MMS1 at ∼0805:53.104 UT). Given that their signatures vary from spacecraft to spacecraft, the wavelengths are not well-determined from the four spacecraft interferometry approach but are expected to be < 11–18 km (or < 0.2–0.3$\lambda_i$). Finally, we report that the cumulative sums of $D_\circ$ from all four spacecraft plateau in the interval spanning the shock overshoot and undershoot regions (not shown), thereby indicating that the primary region of net dissipation of wave energy to the plasma is localized in the ramp.

Figure 2j shows the dynamic energy conversion rate spectra in the plasma rest frame $\tilde{D}_{\circ 1}$ from MMS1 in the frequency range from 0.3 to 15 Hz. The spectra were determined using the expression $\tilde{D}_{\circ 1} = \frac{1}{2}\mathcal{R}\{\widetilde{\mathbf{J}}_{\mathrm{mom1}}(f) \cdot \widetilde{\mathbf{E}}^*_{\circ 1}(f)\}$ (Hull et al., 2020; Swanson, 1989). Here, the dot product is performed in frequency space with Morlet wavelet transformed components of the current density $\widetilde{\mathbf{J}}_{\mathrm{mom1}}(f)$ and the complex conjugate of wavelet transformed components of the plasma frame electric field $\widetilde{\mathbf{E}}^*_{\circ 1}(f)$ from MMS1. The symbol $\mathcal{R}$ denotes the real part. Implicit in $\tilde{D}_{\circ 1}$ is that it represents an average over the wave period resulting in the 1/2 multiplicative factor. The red in Figure 2j indicates negative values for $\tilde{D}_{\circ 1}$ corresponding to energy exchange from the plasma to the waves. The blue indicates positive values, which signify energy exchanged from the LF waves to the plasma. The results show that values for $\tilde{D}_{\circ 1}$ are preferentially negative (red) over the range of frequencies depicted in 2j from the beginning of the interval to about 0805:40 UT. After this interval, localized patches of positive values (blue) for $\tilde{D}_{\circ 1}$ are found to be intermixed with negative values. The trends in the dynamic spectra of $\tilde{D}_{\circ 1}$ are similar to the dynamic spectra of energy conversion rates quantified in the shock NIF $\tilde{D}_{\mathrm{NIF1}} = \frac{1}{2}\mathcal{R}\{\widetilde{\mathbf{J}}_{\mathrm{mom1}}(f) \cdot \widetilde{\mathbf{E}}^*_{\mathrm{NIF1}}(f)\}$ presented in the study by Hull et al. (2020). This indicates that the conversion rates are not significantly altered by differences in the plasma rest frame and shock rest frame transformations for this event, which is not guaranteed owing to the frame dependence of the electric field.

Figure 3 depicts the distribution of conversion rates as a function of scales for fluctuations at $f \lesssim$ a few 10s of Hz in the foot and ramp region. Note, the four spacecraft interferometry method determines scales that are effectively

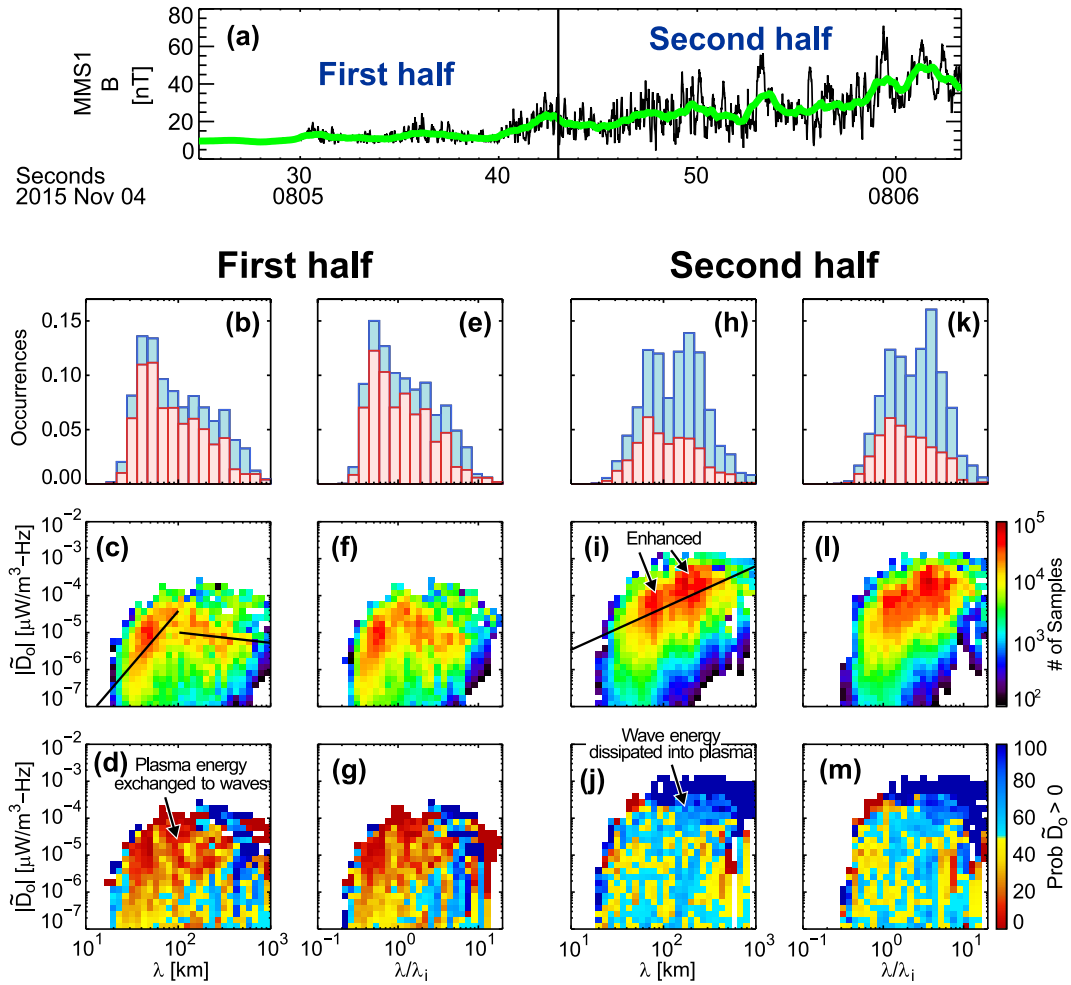


**Figure 3.** (a) Magnetic field magnitude. The black curve indicates burst-sampled observations from FGM, while the green indicates 1 s boxcar averages. Also shown are occurrence distributions of (b, h) wavelengths $\lambda$ and (e, k) wavelengths normalized by the ion inertial length $\lambda/\lambda_i$ color coded according to relative contributions associated with positive (blue) and negative (red) values of energy conversion rate spectral densities $\tilde{D}_\circ$ in plasma frame, distributions of energy conversion rate spectral density amplitudes $|\tilde{D}_\circ|$ in the plasma frame as a function of (c, i) $\lambda$ and (f, l) $\lambda/\lambda_i$, and probability distributions of positive values for $\tilde{D}_\circ$ as a function of (d, j) $|\tilde{D}_\circ|$ and $\lambda$ and (g, m) $|\tilde{D}_\circ|$ and $\lambda/\lambda_i$ for the (b–g) first half and (h–m) the second half of the interval depicted in (a). The solid black lines in (c) and (i) indicate results of a regression analysis applied to the data.

defined at the tetrahedron barycenter. Thus, to assess how they depend on scale we use energy conversion rate spectral densities defined at the barycenter given by $\tilde{D}_\circ = \frac{1}{2}\mathcal{R}\{\widetilde{\mathbf{J}}_{\rm curl}(f)\cdot\widetilde{\mathbf{E}}^*_{\circ\rm BC}(f)\}$. $\widetilde{\mathbf{J}}_{\rm curl}$ is the wavelet transform of the current density determined via the curlometer method (Dunlop et al., 1988) applied to magnetic field measurements and $\widetilde{\mathbf{E}}^*_{\circ\rm BC}$ is the complex conjugate of the wavelet transform of the electric field in the plasma frame defined at the tetrahedron barycenter (Chanteur, 1998). We use $\widetilde{\mathbf{J}}_{\rm curl}$ here since the times match those of the interferometry results and the values extend to higher frequencies than their moment counterpart, which facilitate the comparisons. Additionally, the curlometer current density time series data are generally in reasonably good agreement (typically 26%) with the barycenter averages of moment determined current densities throughout the interval of interest (not shown). The statistical distributions were compiled over the two intervals indicated in Figure 3a, which encompass the foot and ramp region just before the magnetic overshoot. The division of the layer into these two intervals was motivated by the behavior of the conversion rate cumulative sums discussed above. Namely, the division roughly bisects the center of the plateau between decreasing and increasing slopes in Figure 2i. The first half encompasses the upstream part of the foot, while the second half encompasses the rest of the foot and ramp regions, respectively. The occurrence distributions of wavelengths $\lambda$ associated with the two intervals are given in Figures 3b and 3h, respectively. The distributions are based on values of $\lambda$ determined from

the cross-spectral analysis that satisfy the coherency and time-delay criteria discussed above. To place the scales into physical parameter context, the occurrence distribution of wavelength scales normalized by their corresponding local ion inertial length values ($\lambda/\lambda_i$) are also depicted in Figures 3e and 3k, respectively. The red and blue represent the relative occurrence contributions associated with negative and positive values of $\tilde{D}_\circ$, respectively (i.e., total occurrence at a given bin is the sum of the two). Comparisons reveal dramatic differences among the scale occurrence distributions in the two intervals. In the first half, the distribution is enhanced at $\lambda \sim 50 \pm 20$ km (Figure 3b) corresponding to fluctuations at sub-ion inertial length scales ($\lambda/\lambda_i \sim 0.65 \pm 0.35$ in Figure 3e). In contrast, the second half is marked by a double-peaked scale distribution with enhancements at $\sim 75 \pm 25$ km and $\sim 200 \pm 80$ km, respectively (see Figure 3h). Owing to enhanced densities in the interval, these peaks correspond to normalized scales of $\sim \lambda/\lambda_i \sim 1.3 \pm 0.6$ and $\sim \lambda/\lambda_i \sim 4.0 \pm 1.5$, respectively (see Figure 3k). Note, the lower limit of the scale distributions in both regions is artificial in that it reflects the lack of coherent whistler signals being resolved by all four spacecraft, which are at ~11–18 km separations in this interval. On the other hand, the upper range of the scale distribution in each region is physically limited by the intrinsic thickness of the shock foot-ramp region.

The distribution of energy conversion rate spectral density amplitudes $|\tilde{D}_\circ|$ as a function of $\lambda$ and $\lambda/\lambda_i$ are depicted in Figures 3c and 3f for the first half and in Figures 3i and 3l for the second half of the interval. To statistically assess the direction of energy exchange, we also show the probability distributions of positive values of $\tilde{D}_\circ$ as a function of $|\tilde{D}_\circ|$ and $\lambda$ (Figures 3d and 3j) and as a function of $|\tilde{D}_\circ|$ and $\lambda/\lambda_i$ (Figures 3g and 3m) in the two intervals. Note, percentages above 50% within a given bin indicate preferential positive values for $\tilde{D}_\circ$ (cyan to blue), corresponding to wave energy dissipation into the plasma. Values below 50% indicate preferential negative values for $\tilde{D}_\circ$ (yellow to red), corresponding to energy extraction from the plasma to the waves.

In the first half of the interval, the values for $|\tilde{D}_\circ|$ are relatively small reaching $\sim 10^{-4}$ $\mu$W/(m$^3$Hz) in Figures 3c and 3f. The dominant contributions to the 2D distribution come from the fluctuations at ~30–100 km wavelength scales (or $\lambda/\lambda_i \sim 0.3 - 1.0$). The $|\tilde{D}_\circ|$ values in this range exhibit a sharp increase with increasing scale from $\sim 10^{-6}$ to $\sim 10^{-4}$ $\mu$W/(m$^3$Hz). Important contributions also come from samples at longer wavelengths (e.g., yellow to orange in Figure 3c at $\lambda > 100$ km). However, in this range the $|\tilde{D}_\circ|$ values show a slower decrease with increasing scale. The solid black lines in Figure 3c indicate the results of a log space linear regression analysis applied to the data in the wavelength ranges $\lambda < 100$ km and $\lambda \geq 100$ km. The analysis resulted in the power law relations $|\tilde{D}_\circ^{\text{foot}}| = 10^{-10.3}\lambda^{2.9}$ for $\lambda < 100$ km and $|\tilde{D}_\circ^{\text{foot}}| = 10^{-4.4}\lambda^{-0.28}$ for $\lambda \geq 100$ km, respectively. Figures 3d and 3g demonstrate that the important contributions over the full range of scales are generally associated with energy exchange from the plasma to the waves (yellow to red). This is also exhibited in the occurrence distributions shown Figures 3b and 3e, which demonstrate the predominance of negative conversion rate contributions (red), with little contributions associated with positive values (blue). An exception occurs at the largest scales, which exhibit some evidence of energy dissipation to the plasma (cyan to blue in Figures 3d and 3g). However, these are associated with reduced occurrences as demonstrated in Figures 3b and 3e.

In the second half of the layer, the 2D histograms shown in Figures 3h and 3i reveal strong increases in $|\tilde{D}_\circ|$ across all scales, with the most dramatic increase occurring at wavelengths above 100 km. The enhanced $|\tilde{D}_\circ|$ values are due to intensified current densities (and also electric fields). In contrast to the first half counterparts, the 2D histograms in the second half reveal that $|\tilde{D}_\circ|$ is positively correlated with $\lambda$ and $\lambda/\lambda_i$ at all scales, with linear correlation coefficients for both comparisons determined at $r = 0.55$. Regression analysis resulted in the power law scaling relation $|\tilde{D}_\circ^{\text{ramp}}| = 10^{-6.6}\lambda^{1.1}$ (black line in Figure 3i). The probability distributions in Figures 3j and 3m indicate that energy is being preferentially exchanged from the waves to the plasma (cyan to blue) at larger scales ($\lambda \gtrsim 100$ km or $\lambda/\lambda_i \gtrsim 2$). Dissipation of energy occurs at shorter scales but it is unclear whether it dominates. This is clarified in Figures 3h and 3k, which show that preferential dissipation of wave energy (more blue than red) is exhibited at scales $\lambda \gtrsim 120$ km or $\lambda/\lambda_i \gtrsim 2$ (encompassing the second peak), whereas at the shorter scales (first peak) the energy conversion is more balanced (equal blue and red levels).

### 3.3. Poynting Fluxes

Whistler waves can, through Poynting flux, carry energy to different parts of the shock layer, where it can be dissipated into plasma heating. Figure 4 shows Poynting fluxes observed by MMS1 within the foot and ramp

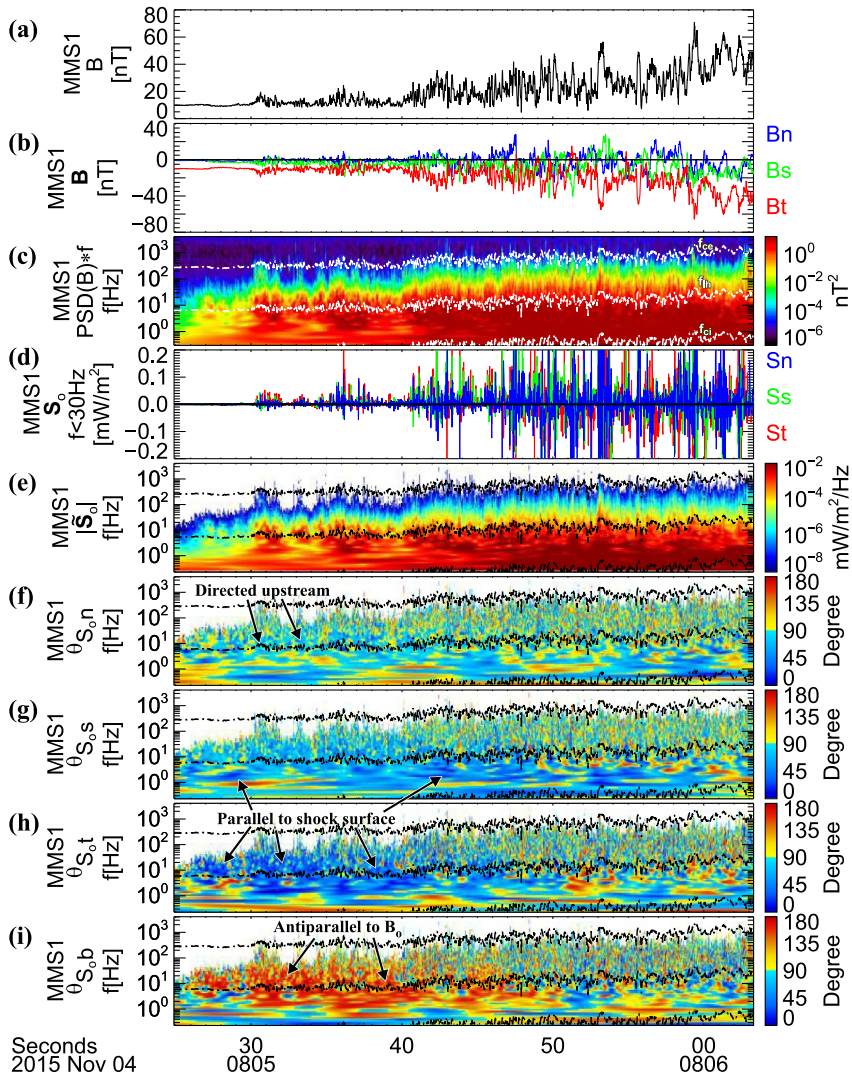


**Figure 4.** Observations from MMS1. Shows (a) Magnetic field magnitude, (b) magnetic field vector in the shock nst coordinates, (c) normalized magnetic field power spectral densities, (d) Poynting fluxes $\mathbf{S}_{o1}$ at $f < 30$ Hz in the plasma rest frame, (e) spectra of $|\widetilde{\mathbf{S}}_{o1}|$, and the spectra of the angle between $\widetilde{\mathbf{S}}_{o1}$ and (f) the shock normal $\hat{\mathbf{n}}$, (g) $\hat{\mathbf{s}}$, (h) $\hat{\mathbf{t}}$ and (i) the background magnetic field, respectively. The ion cyclotron ($f_{ci}$), lower-hybrid ($f_{lh}$), and electron cyclotron ($f_{ce}$) frequencies are indicated by the white curves in (c) and black curves in (e)–(i), respectively.

region of the 04 November 2015 0805 UT shock crossing. Figure 4d displays the time series of Poynting fluxes at frequencies <30 Hz in the plasma rest frame transformed into a shock geometry-based nst coordinate system defined by the orthonormal basis unit vectors: $\hat{\mathbf{n}}$, which is along the upstream directed shock normal, $\hat{\mathbf{s}}$, which is parallel to the shock surface transverse to the magnetic coplanarity plane, and $\hat{\mathbf{t}}$, which is in the coplanarity plane parallel to the shock surface. For this event, $\hat{\mathbf{n}} = [0.9867, 0.1615, -0.01916]$ is nearly along GSE-$x$, $\hat{\mathbf{s}} = [-0.0267, 0.2773, 0.9604]$ is nearly along GSE-$z$, and $\hat{\mathbf{t}} = [0.1604, -0.9471, 0.2779]$ is nearly antiparallel to GSE-$y$ (from Hull et al., 2020). The plasma frame Poynting flux vector estimated from MMS1 time series observations is defined as $\mathbf{S}_{o1} = \mathbf{E}_{o1} \times \mathbf{B}_1/\mu_0$. The electric and magnetic fields were low-pass filtered at 30 Hz before computing $\mathbf{S}_{o1}$.

To examine contributions as a function of frequency, Figure 4e shows the dynamic frequency spectra of plasma frame Poynting flux spectral density amplitudes $|\widetilde{\mathbf{S}}_{o1}|$ from MMS1. The plasma frame Poynting flux vector spectral densities were determined from the expression $\widetilde{\mathbf{S}}_{o1} = \mathcal{R}\{\widetilde{\mathbf{E}}_{o1}(f) \times \widetilde{\mathbf{B}}_1^*(f)\}/(2\mu_0)$ (LeDoc, 1998; Swanson, 1989). The cross product is performed in frequency space via Morlet wavelet transformed components of the

plasma frame electric field vector $\widetilde{\mathbf{E}}_{\circ 1}$ and the complex conjugate of wavelet transformed components of the magnetic field vector $\widetilde{\mathbf{B}}_1^*$ sampled by MMS1. Though we are focused on fluctuations below 30 Hz, the spectra were quantified and shown for frequencies up to the 4 kHz Nyquist limit of the burst sampled fields for contextual purposes. To get a sense of the direction of energy transport relative to the shock geometry, Figures 4f–4h displays dynamic spectra of the angles between the plasma rest frame Poynting flux vector $\widetilde{\mathbf{S}}_{\circ 1}$ and the unit vectors $\hat{\mathbf{n}}$, $\hat{\mathbf{s}}$, and $\hat{\mathbf{t}}$, respectively. Finally, the dynamic spectra of the angles between the plasma frame Poynting flux vector and the background magnetic field $\mathbf{B}_{01}$ (dynamically determined for each $f$) are given in Figure 4i. For context, the magnetic field amplitude and vector components in nst coordinates from MMS1 are shown in Figures 4a and 4b. In the shock nst coordinates, the largest component is $B_{t1}$, with the other two components being generally smaller, which is characteristic of a quasiperpendicular shock. Hull et al. (2020, Figure A1d) demonstrated that the magnetic field along the normal at shock macro-scales is approximately constant. On the upstream asymptotic side, the magnetic field vector points into the shock, since the component along the upstream directed normal is negative ($B_{n1}^{\mathrm{up}} \sim -1$ nT). Here, it is apparent that the superposed whistler activity results in significant excursions from constancy, owing to their large amplitudes. This underscores the importance of defining the background field as a function frequency when organizing spectral data by the field. In addition to these quantities, the normalized magnetic field PSD is also provided for context in Figure 4c.

Similar to the behavior of energy conversion rates discussed in Section 3.2, Figure 4d reveals that the Poynting fluxes are bursty in nature with intensities increasing with increasing penetration into the layer. The amplitudes range from a few tenths to a few hundredths of mW/m$^2$. Figure 4e indicates that Poynting fluxes arise from fluctuations extending over a broad frequency range from sub-hertz to several hundred Hz, which span the frequencies of whistler waves within the layer. The $|\widetilde{\mathbf{S}}_{\circ 1}|$ are largest at lower frequencies with values reaching $\gtrsim 10^{-2}$ mW/m$^2$Hz and diminishing significantly to $\lesssim 10^{-5}$ mW/m$^2$Hz at several 10–100s of Hz. Figures 4g and 4h reveal that the plasma frame Poynting fluxes at frequencies $\gtrsim$1 Hz are primarily oriented along the shock surface, being preferentially oriented within the coplanarity plane (along $\hat{\mathbf{t}}$) indicated by the darker blue in Figure 4h from 0805:24-0805:42 UT and subsequently transitioning to the out-of-coplanarity direction (along $\hat{\mathbf{s}}$) indicated by darker blue in Figure 4g. As a consequence of being aligned along the shock surface, the plasma frame Poynting fluxes are nearly antiparallel to $\mathbf{B}_{01}$ (see Figure 4i). The plasma frame Poynting fluxes are generally quasi-perpendicular with respect to the shock normal but have a slight upstream tendency as indicated by the cyan in Figure 4f.

To assess the ability of associated whistler waves to transport energy to different parts of the shock and hence their impact, it is important to examine Poynting flux behavior in a relevant shock frame of reference. Figure 5 displays Poynting fluxes from MMS1 transformed into the NIF in the same format as Figure 4. The NIF is the shock rest frame of reference in which the upstream bulk velocity is aligned along the shock normal. The Poynting flux vector in this frame estimated from time series observations is defined as $\mathbf{S}_{\mathrm{NIF1}} = \mathbf{E}_{\mathrm{NIF1}} \times \mathbf{B}_1/\mu_0$. The electric field in the NIF is derived from its spacecraft frame counterpart via the relation $\mathbf{E}_{\mathrm{NIF1}} = \mathbf{E}_{\mathrm{SC1}} + (v_{\mathrm{sh}}\hat{\mathbf{n}} + \mathbf{v}_{\mathrm{NIF}}) \times \mathbf{B}_1$, where $\mathbf{v}_{\mathrm{NIF}} = \hat{\mathbf{n}} \times (\mathbf{V}_{\mathrm{SW}} \times \hat{\mathbf{n}})$, $v_{\mathrm{sh}}$ is the relative velocity along the shock normal, and $\mathbf{V}_{\mathrm{SW}}$ the solar wind velocity. The components of $\mathbf{S}_{\mathrm{NIF1}}$ at frequencies <30 Hz in nst coordinates is shown in Figure 5d.

The NIF Poynting flux vector spectral density from MMS1 is given by the relation $\widetilde{\mathbf{S}}_{\mathrm{NIF1}} = \mathcal{R}\{\widetilde{\mathbf{E}}_{\mathrm{NIF1}} \times \widetilde{\mathbf{B}}_1^*\}/(2\mu_0)$. The magnitudes $|\widetilde{\mathbf{S}}_{\mathrm{NIF1}}|$ versus frequency are shown in Figure 5e, which are very similar to their plasma frame counterparts shown in Figure 4e. Figures 5g and 5h reveal that the NIF Poynting fluxes at $\gtrsim$ 1 Hz frequencies remain primarily along the shock surface, with orientations that are similar to their plasma frame counterparts. Namely, the Poynting fluxes are preferentially inclined within the coplanarity plane along $\hat{\mathbf{t}}$ from 0805:24-0805:42 UT (dark blue in Figure 5h) but are preferentially in the out-of-coplanarity direction $\hat{\mathbf{s}}$ afterward (dark blue in Figure 5g). Though the Poynting fluxes projected along the shock surface rotate with increasing penetration into the layer, they remain quasi-antiparallel to the magnetic field (red in Figure 5i). In contrast to the plasma frame, Figure 5f indicates that the NIF Poynting fluxes at ∼10 Hz and below are quasiperpendicular to the shock normal with a downstream directed preference (yellow to orange). This is also indicated in Figure 5d, which shows the NIF Poynting fluxes along the normal are generally smaller than the other two components and have a notable negative bias. There is evidence of the NIF Poynting fluxes along the normal at higher frequencies alternating between slightly upstream (cyan) and sightly downstream (yellow) orientations (more so in the second half of Figure 5f).

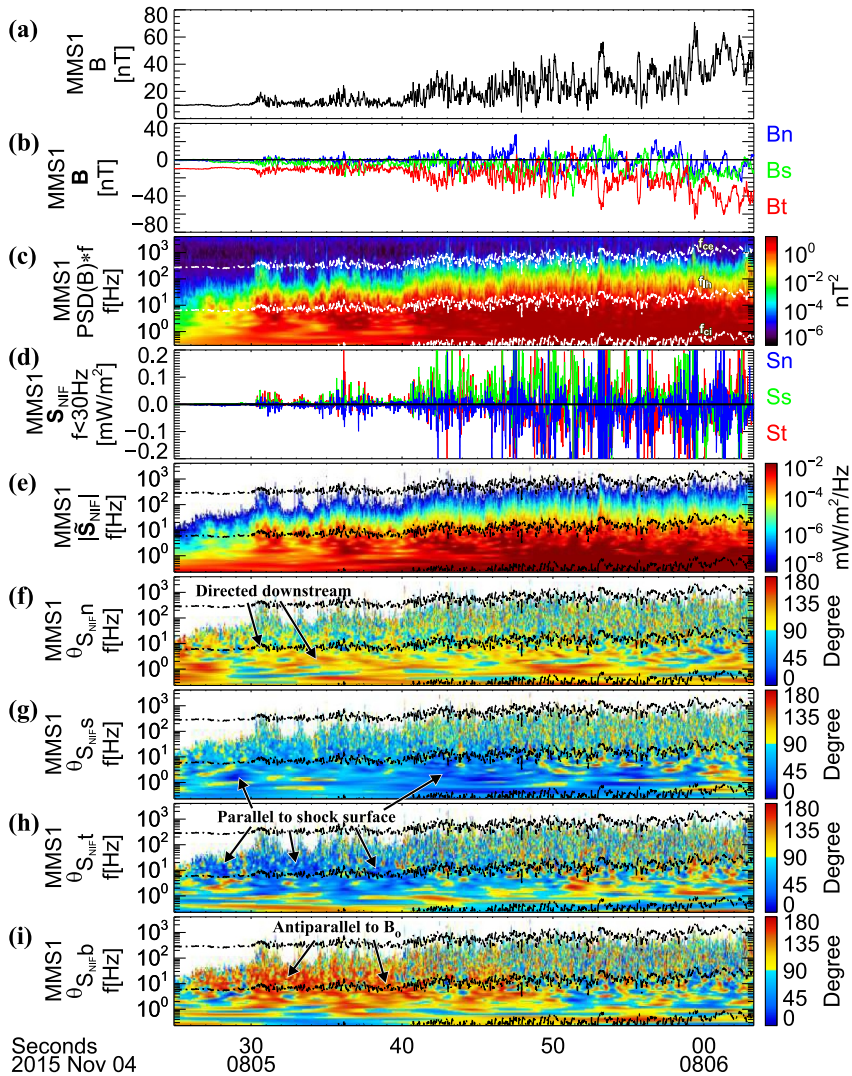


**Figure 5.** Observations from MMS1. Shows (a) Magnetic field magnitude, (b) magnetic field vector in the shock nst coordinates, (c) normalized magnetic field power spectral densities, (d) Poynting fluxes $\mathbf{S}_{\mathrm{NIF1}}$ at $f < 30$ Hz in the shock rest frame, (e) spectrograms of $|\widetilde{\mathbf{S}}_{\mathrm{NIF1}}|$, and spectrograms of the angle between $\widetilde{\mathbf{S}}_{\mathrm{NIF1}}$ and (f) the shock normal $\hat{\mathbf{n}}$, (g) $\hat{\mathbf{s}}$, (h) $\hat{\mathbf{t}}$ and (i) the background magnetic field, respectively. The ion cyclotron ($f_{\mathrm{ci}}$), lower-hybrid ($f_{\mathrm{lh}}$), and electron cyclotron ($f_{\mathrm{ce}}$) frequencies are indicated by the white curves in (c) and black curves in (e)–(i), respectively.

To examine the spatial and temporal nature of wave energy transport, Figure 6 displays the cumulative sums of the Poynting fluxes below 30 Hz measured by each of the MMS spacecraft in the foot and ramp region of the shock. Figures 6b–6d show the cumulative sums of $S_{on}$, $S_{os}$, and $S_{ot}$, which are Poynting fluxes below 30 Hz in the plasma frame projected along $\hat{\mathbf{n}}$, $\hat{\mathbf{s}}$, and $\hat{\mathbf{t}}$, respectively. The net increase or decrease (i.e., positive or negative slope) in these values provides essential information on the overall preferred directionality of energy flow associated with the fluctuations below 30 Hz in the interval. In the first half of the interval, there is a strong positive increase in the cumulative sums of $S_{ot}$, with much smaller increases in the sums of $S_{on}$ and $S_{os}$. This confirms that the transport of energy in the plasma frame is predominantly parallel to the shock surface within the coplanarity plane antiparallel to the magnetic field and with a slight upstream directed preference surmised above. Consistent with the coherent nature of the LF whistlers, the observed increases in the cumulative sums of $S_{on}$, $S_{os}$, and $S_{ot}$ in this region are also roughly the same for all four spacecraft. With increasing penetration deeper into the ramp, the energy transport is still primarily parallel to the shock surface but transitions to being primarily in the out-of-coplanarity direction $\hat{\mathbf{s}}$ (second half of the interval in Figure 6c). The cumulative sums of $S_{ot}$ plateau and eventually decrease near the end of the interval in Figure 6d indicating a reversal in the direction of energy flow along $\hat{\mathbf{t}}$. Similar to what was found

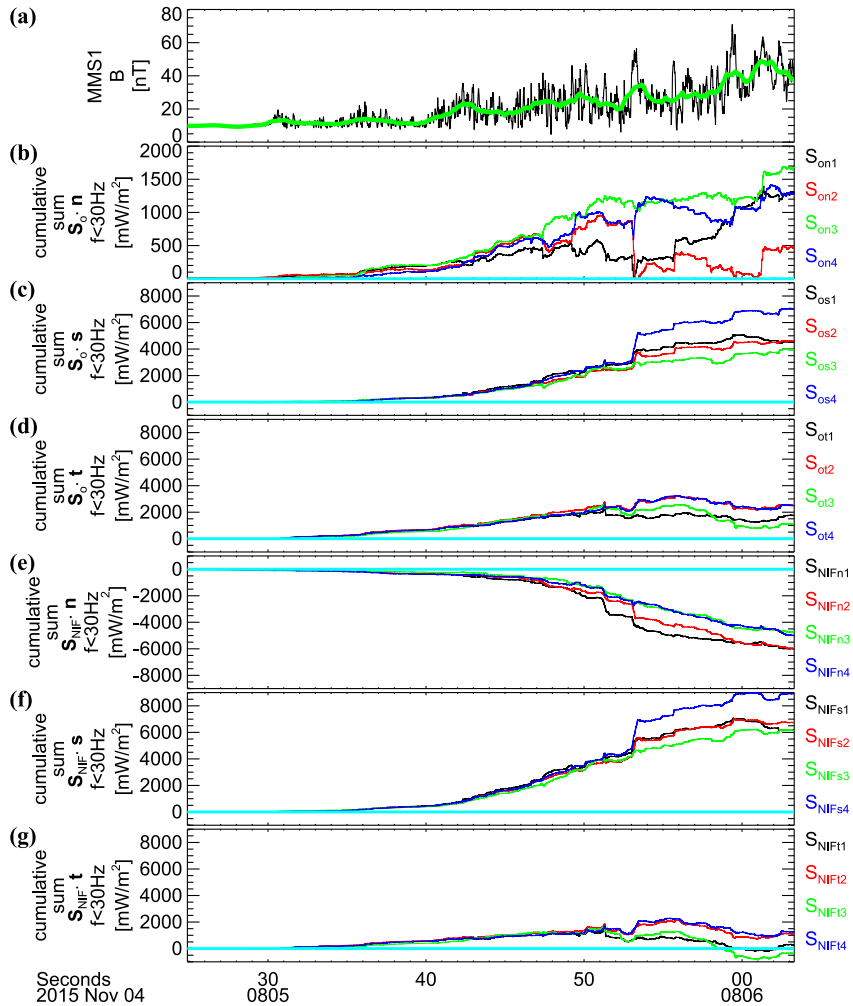


**Figure 6.** (a) Magnetic field magnitude measured by MMS1, the cumulative sums of plasma frame Poynting fluxes projected along (b) $\hat{\mathbf{n}}$, (c) $\hat{\mathbf{s}}$, and (d) $\hat{\mathbf{t}}$, and the cumulative sums of shock NIF Poynting fluxes projected along (e) $\hat{\mathbf{n}}$, (f) $\hat{\mathbf{s}}$, and (g) $\hat{\mathbf{t}}$. The cyan line in (b)–(g) indicates where the cumulative sums are zero. To make the trends more visible, panel (b) has a reduced *y*-axis range relative to (c)–(g).

for energy conversion rates, the sums of $S_{os}$ and $S_{ot}$ do exhibit departures among spacecraft comparisons in the ramp that arise from gross differences in slopes with some superposed localized steps. Departures are most notable in the sums of $S_{on}$ in the second half (Figure 6b), owing to the much smaller amplitudes relative to the other two components. Despite the variability, the cumulative sums of $S_{on}$ exhibit a slight increasing trend in MMS1, MMS3, and MMS4 data; however, the trend for MMS2 is unclear. The variability in the cumulative sums of $S_{on}$, $S_{os}$ and $S_{ot}$ deeper in the ramp is related to that found in energy conversion rate sums described above in Section 3.2 and is consequent to spatial and temporal variations in the whistler wave electric and magnetic fields within the short spatial separations of the MMS spacecraft.

To assess their behavior relative to a shock rest frame, Figures 6e–6g show the cumulative sums of $S_{\mathrm{NIF}n}$, $S_{\mathrm{NIF}s}$, and $S_{\mathrm{NIF}t}$, which are Poynting fluxes below 30 Hz in the shock NIF projected along $\hat{\mathbf{n}}$, $\hat{\mathbf{s}}$, and $\hat{\mathbf{t}}$, respectively. In this frame, we still see that the energy transport is predominantly parallel to the shock surface. This transport of energy is within the coplanarity plane along $\hat{\mathbf{t}}$ in the first half of the layer (Figure 6g) but later is dominantly in the out-of-coplanarity direction (Figure 6f), as was observed in the plasma rest frame case. However, the cumulative sums of $S_{\mathrm{NIF}n}$ have the opposite sign to their plasma frame counterparts, indicating that the gross energy flow and thus group velocities have a downstream directed sense in the shock NIF.

To examine dependencies on scales, Figure 7 shows distributions of Poynting flux spectral densities as a function of wavelengths for coherent fluctuations at a few tens of Hertz and below. Note, Poynting flux spectral densities in both the rest frame and NIF were determined using wavelet transformed electric and magnetic fields defined at the tetrahedron barycenter for these comparisons. Specifically, $\widetilde{\mathbf{S}}_{\circ} = \mathcal{R}\{\widetilde{\mathbf{E}}_{\circ BC} \times \widetilde{\mathbf{B}}^{*}_{BC}\}/(2\mu_0)$ and $\widetilde{\mathbf{S}}_{NIF} = \mathcal{R}\{\widetilde{\mathbf{E}}^{BC}_{NIF} \times \widetilde{\mathbf{B}}^{*}_{BC}\}/(2\mu_0)$. The statistical distributions were again compiled over the two intervals indicated in Figure 7a. For context, the occurrence distributions of $\lambda$ associated with the two intervals are given in Figures 7b and 7n, respectively. The corresponding occurrence distributions of $\lambda/\lambda_i$ are depicted in Figures 7h and 7t, respectively. The color code indicates the relative occurrence contributions associated with positive (blue) and negative (red) values of $\tilde{S}_{on}$, corresponding to upstream and downstream directed sense, respectively.

The distribution of plasma rest frame Poynting flux spectral density amplitudes $|\widetilde{\mathbf{S}}_{o}|$ versus $\lambda$ and $\lambda/\lambda_i$ are given in Figures 7c and 7i for the first half and in Figures 7o and 7u for the second half of the interval. Also shown are the probability distributions of positive rest frame Poynting fluxes projected along the shock normal $\tilde{S}_{on}$ as a function of $|\widetilde{\mathbf{S}}_{o}|$ versus $\lambda$ (Figures 7d and 7p) and as a function of $|\widetilde{\mathbf{S}}_{o}|$ and $\lambda/\lambda_i$ (Figures 7j and 7v) in the two intervals. Note, percentages above 50% within a given bin indicate values for $\tilde{S}_{on}$ that are preferentially positive (cyan to blue), signifying preferential upstream directed energy transport in the plasma frame. Values below 50% indicate preferential negative values for $\tilde{S}_{on}$ (yellow to red), signifying energy transport that is preferentially directed downstream.

The scale dependence of Poynting fluxes associated with LF whistler fluctuations shows similar behavior as the energy conversion rate dependencies previously discussed. Particularly, in the first half of the interval, values for $|\widetilde{\mathbf{S}}_{o}|$ at $\lambda \sim$30–100 km (or $\lambda/\lambda_i \sim 0.3 - 1.0$) increase with increasing scale, peaking at $\sim 1\text{–}2 \times 10^{-3}$ mW/(m$^2$Hz). Regression analysis applied to this wavelength range yielded the power law scaling relation $|\widetilde{\mathbf{S}}^{foot}_{o}| = 10^{-9.4}\lambda^{3.1}$ (black line in Figure 7c). At longer wavelengths ($\lambda > 100$ km or $\lambda/\lambda_i > 1.0$), values for $|\widetilde{\mathbf{S}}_{o}|$ are reduced from peak amplitudes, however, the trend is unclear owing to changing slopes. Values for $|\widetilde{\mathbf{S}}_{o}|$ in the second half of the interval are significantly enhanced (reaching $\sim 1\text{–}3 \times 10^{-2}$ mW/(m$^2$Hz)) and found to be positively correlated with $\lambda$ and $\lambda/\lambda_i$ at all scales, with coefficients of $r = 0.59$ and $r = 0.58$ for comparisons shown in Figures 7o and 7u, respectively. Regression analysis applied to the full wavelength range yielded the power law scaling relation $|\widetilde{\mathbf{S}}^{ramp}_{o}| = 10^{-6.3}\lambda^{1.7}$ (black line in Figure 7o). The probability distributions shown in Figures 7d and 7p (also in Figures 7j and 7v) statistically demonstrate that the Poynting fluxes across the resolved scales in both intervals are preferentially directed upstream in the plasma frame. This is further clarified in Figures 7b and 7n (also in Figures 7h and 7t), where the largest occurrence contributions across most scales are associated with upstream directed Poynting fluxes in the plasma frame (indicated in blue) in both intervals.

To examine dependencies in the NIF, the occurrence distribution of $\lambda$ and $\lambda/\lambda_i$ color coded according to relative contributions associated with positive (blue) and negative (red) values of $\tilde{S}_{NIFn}$ are given in Figures 7e and 7k in the first half and Figures 7q and 7w in the second have of the interval, respectively. Additionally, the distributions of the NIF Poynting flux spectral density amplitudes $|\widetilde{\mathbf{S}}_{NIF}|$ as a function of $\lambda$ and $\lambda/\lambda_i$ are shown for the first (Figures 7f and 7l) and second (Figures 7r and 7x) halves of the interval, respectively. The corresponding probability distributions of the Poynting flux spectral densities projected along the shock normal $\tilde{S}_{NIFn}$ as a function of $|\widetilde{\mathbf{S}}_{NIF}|$ and $\lambda$ are depicted in Figures 7g and 7s and as a function of $|\widetilde{\mathbf{S}}_{NIF}|$ and $\lambda/\lambda_i$ in Figures 7m and 7y.

The scale dependencies of $|\widetilde{\mathbf{S}}_{NIF}|$ in the two intervals (Figures 7f, 7l, 7r, and 7x) do not show any marked differences from the plasma rest frame counterpart (Figures 7c, 7i, 7o, and 7u). Regression analysis yielded similar power law relations $|\widetilde{\mathbf{S}}^{foot}_{NIF}| = 10^{-9.5}\lambda^{3.2}$ at $\lambda \sim 0.3 - 1.0\lambda_i$ and $|\widetilde{\mathbf{S}}^{ramp}_{NIF}| = 10^{-6.4}\lambda^{1.8}$ over the full wavelength range in the first and second half of the interval, respectively (black lines in Figures 7f and 7r). This indicates that the frame transformation did not significantly affect the scaling relations. However, the probability distributions in the NIF statistically show the opposite trend. Namely, the NIF Poynting fluxes projected along the normal in both intervals have a preferential downstream directed sense across all resolved scales indicated by the predominance of yellow to red in Figures 7g, 7m, 7s, and 7y. These results are complemented by the occurrence distributions versus $\lambda$ (Figures 7e and 7q) and $\lambda/\lambda_i$ (Figures 7k and 7w), which show that the relative contributions associated with downstream directed Poynting fluxes in the NIF (indicated by red) generally predominate their upstream directed counterpart (indicated by blue) in both intervals.

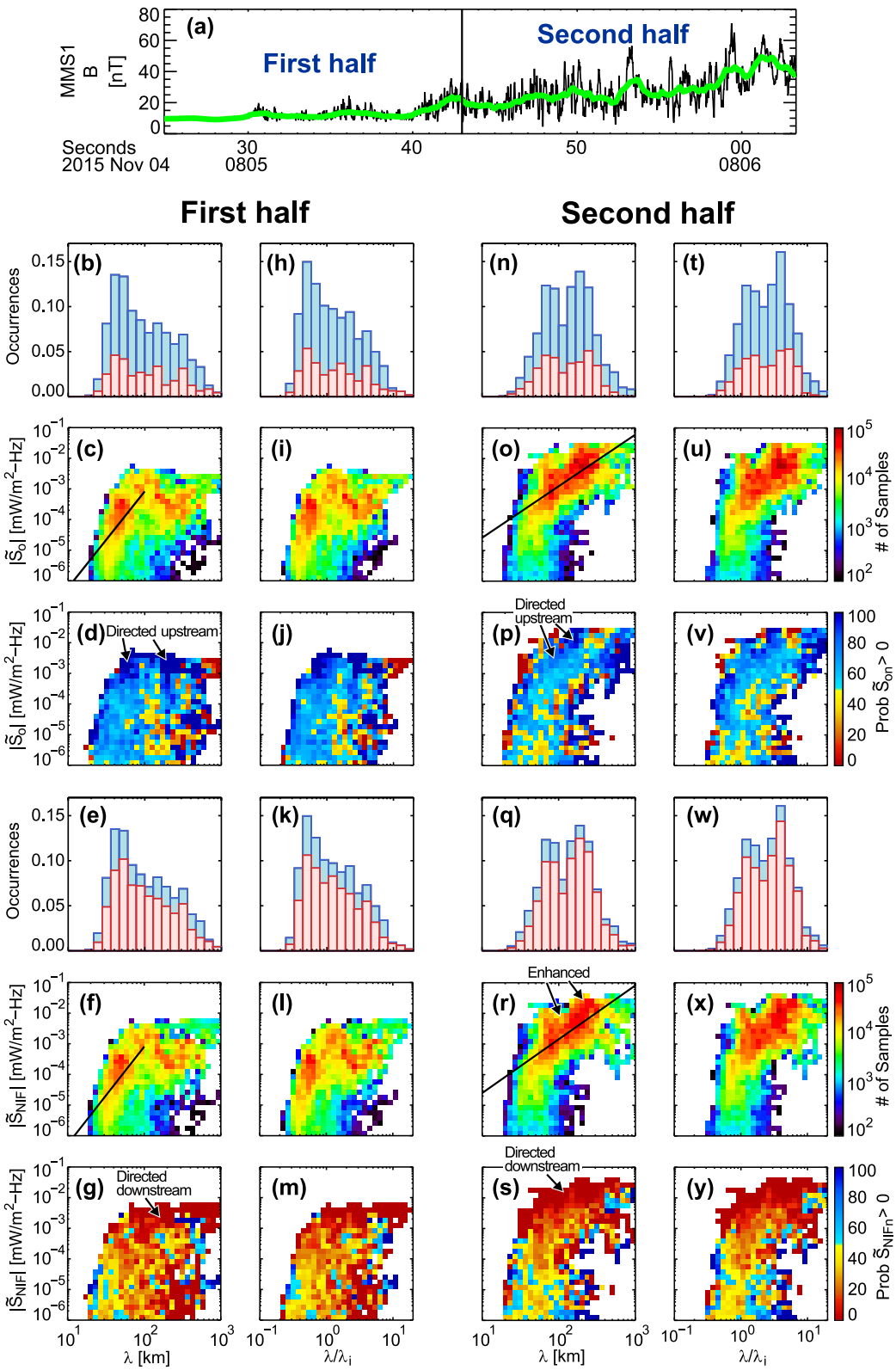


**Figure 7.**

## 4. Discussion

Our results underscore the importance of examining Poynting fluxes in the plasma frame as an additional means for discriminating source mechanisms of the carrier whistler waves. A favored instability candidate for whistlers near lower-hybrid frequencies at quasiperpendicular shocks is the modified two-stream instability (MTSI; also known as the kinetic cross-field streaming instability Wu et al., 1983). The predominantly upstream-directed nature of the plasma rest frame Poynting fluxes discounts the MTSI-slow drift mechanism (MTSI-SD, also referred to as MTSI1 by Matsukiyo & Scholer, 2006) as the source for the LH whistler waves within the foot and ramp region of the shock. The MTSI-SD mechanism, which derives its free energy source from the relatively slow drift between incoming solar wind ions and electrons, is expected to have downstream directed Poynting fluxes in the plasma frame. Moreover, the MTSI-SD mechanism excites whistlers near LH frequencies with wavelengths several times the electron inertial length and that propagate (in the plasma frame) toward the ramp nearly perpendicular to the background magnetic field, which is at odds with the interferometry results reported in Section 3.1. On the other hand, the upstream-directed nature is consistent with the MTSI-fast drift (FD) mechanism, which derives its free energy source from the relatively fast drift between the reflected ions and electrons (also referred to as MTSI2 by Matsukiyo & Scholer, 2006). For a detailed demonstration of the Poynting flux and group velocity expectations for the MTSI-FD case in the plasma and shock frames that are consistent with the observations, see Appendix A. This mechanism is further supported by the results reported by Hull et al. (2020), who demonstrated that the wave vectors are oriented toward the reflected ion beam in such a way as to satisfy the Cerenkov resonance condition in this shock event. The recent study by Lalti et al. (2022) demonstrated this to also be the case at moderate fast mode Mach number quasiperpendicular shocks, supporting the MTSI-FD as the mechanism for that generation of LH whistlers observed at those shocks. Note, upstream-directed Poynting fluxes are also consistent with the dispersive radiation mechanisms as the source of the associated carrier whistler waves (Sundkvist et al., 2012). However, the obliquity of the wave vectors with respect to the shock normal (i.e., not inclined toward the normal), their connectivity with the reflected ion beam demonstrated in Hull et al. (2020), and associated energy conversion rate trends (i.e., generation in upstream part of the foot and absorption in the ramp) discount this as the mechanism for the LF whistlers reported herein.

Our results differ significantly from the results of Sundkvist et al. (2012) who reported on the properties of Poynting fluxes at two quasiperpendicular shocks encountered by the Cluster spacecraft. First, the peak NIF Poynting flux spectral densities reported in Figure 5e are much larger (by one to two orders of magnitude) than those reported by Sundkvist et al. (2012). Second, they reported Poynting flux spectral densities that are preferentially oriented along the shock surface but with an upstream sense in the NIF, which is opposite to our results. These differences are not fully understood but may be due to differing upstream solar wind conditions, such as the fast mode Mach number or the dynamic pressure. Our shock event is characterized by $M_f \sim 6.7$ and $P_{SW} \sim 7$ nPa. Both events reported by Sundkvist et al. (2012) are associated with low values for the solar wind dynamic pressure (obtained from OMNIWEB), with $P_{SW} \sim 2.4$ nPa and $P_{SW} \sim 1.9$ nPa for the first and second event, respectively. The $M_f$ was not reported for the first event, but it is expected to be lower than ours given that $M_A \sim 5.5$. The second event was reported to have $M_f \sim 5$ (according to Lobzin et al., 2007), with $M_A \sim 11$. These comparisons imply that energy reconfiguration may be fundamentally different, with radiation upstream of the shock occurring under lower fast mode Mach number/solar wind dynamic pressure conditions, but with transport and accumulation of energy toward and within the ramp in high Mach number/solar wind dynamic conditions. Verification of this scenario will require the analysis of additional events, which is outside the scope of this paper.

A natural explanation for the conversion rate dependence on location that is revealed in these observations is provided by the characteristics of the MTSI-FD. The excited LF whistlers result from a competition between their destabilizing by the reflected ion beam and their Landau damping by the electrons (Muschietti & Lembège, 2017b). The damping is effected by the parallel component of the wave electric field and depends on the number of electrons in Cerenkov resonance with the wave $\omega = k_{\|} v_{\|}$. This damping increases with a rising electron

**Figure 7.** (a) Magnetic field magnitude. Also shows occurrence distributions of (b, e, n, and q) $\lambda$ and (h, k, t and w) $\lambda/\lambda_i$ color coded according to relative contributions associated with positive (blue) and negative (red) values of (b, h, n, and t) $\tilde{S}_{on}$ and (e, k, q, and w) $\tilde{S}_{\mathrm{NIF}n}$, respectively, distributions of $|\widetilde{\mathbf{S}}_{\mathrm{o}}|$ as a function of (c, o) $\lambda$ and (i, u) $\lambda/\lambda_i$, the probability distributions of positive values of $\tilde{S}_{on}$ as a function of (d, p) $|\widetilde{\mathbf{S}}_{\mathrm{o}}|$ and $\lambda$ and (j, v) $|\widetilde{\mathbf{S}}_{\mathrm{o}}|$ and $\lambda/\lambda_i$, distributions of $|\widetilde{\mathbf{S}}_{\mathrm{NIF}}|$ as a function of (f, r) $\lambda$ and (l, x) $\lambda/\lambda_i$, the probability distributions of positive values of $\tilde{S}_{\mathrm{NIF}n}$ as a function of (g, s) $|\widetilde{\mathbf{S}}_{\mathrm{NIF}}|$ and $\lambda$ and as a function of (m, y) $|\widetilde{\mathbf{S}}_{\mathrm{NIF}}|$ and $\lambda/\lambda_i$ for the (b–m) first half and (n–y) the second half of the combined foot/ramp region depicted in (a). The solid black lines in (c), (f), (o), and (r) indicate results of a regression analysis applied to the data.

temperature (Muschietti & Lembège, 2017b, Figure 5). Using parameter values appropriate for the observations, $k\lambda_i = 10$, $\theta_{kb} = 120°$, we find that the Landau damping of whistlers with $\omega/k_{\|} = 800$ km/s increases by a factor of two where the electron temperature $T_e$ rises from 20 to 60 eV. In the upstream section of the foot, the electrons are relatively cold (median temperature ~20 eV), so that the instability can take place and energy gets transferred to the waves. On the other hand, closer to the ramp $T_e$ increases substantially, whereas the relative drift $|\mathbf{V_b}|$ decreases, the specular reflection point being reached in the ramp. In our case, electron heating is relatively strong, with the electron temperature reaching $T_e \sim 140$ eV at the magnetic overshoot. As a result of these effects, energy conversion goes in the other direction. Namely, wave energy gets dissipated into plasma heating, specifically electron heating. The observations of Poynting fluxes in the NIF demonstrate energy transport is aligned along the surface, with smaller downstream directed sense, suggesting that the group propagation of the spectrum of wave packets is back toward the layer but mostly along its surfaces.

The interaction of the packets with increasing magnetic field and density gradients may result in accumulation and ducting along the surface, owing to reflection analogous to ducting in the magnetosphere. This can have the effect of increasing the interaction scale to be much longer than the layer's width. This suggests the following scenario. Whistler waves are excited in the upstream section of the foot. However, owing to the high solar wind velocity, the waves are unable to group propagate upstream or stand in the flow in a frame fixed with respect to the shock. The broad spectrum of wave packets are slowly carried back toward the ramp where they pile up and interfere with each other creating the wave mix observed, and the energy they carry gets dissipated into electron heating. Moreover, the expectation that the Landau damping effect first eliminates the shorter wavelengths is consistent with the observed trend of larger normalized wavelength scales being observed deeper in the ramp.

## 5. Summary and Conclusions

In this study, we utilized multipoint measurements from MMS within the foot and ramp of a high Mach number quasiperpendicular shock to analyze the properties of intense whistler waves near lower hybrid frequencies and below, the Poynting fluxes these waves carry, and associated energy conversion rates, including their spatial-temporal behavior and dependencies on scale. We employed a four spacecraft wavelet-based interferometry technique to dynamically determine the coherency and characteristic parameters of these LF whistlers. In addition to providing accurate determinations of the phase speeds and rest frame frequencies, this approach also yielded accurate estimates of wavelengths. We used this information to determine, for the first time, the scale distribution and hence the scale dependency of the Poynting fluxes and energy conversion rates associated with the LF whistler wave fluctuations.

The cross-spectral analysis results indicate that the whistlers at frequencies up to several tens of Hz in the first half and up to ~10 Hz in the second half of the layer are generally "coherent". With some exceptions, the whistlers at higher frequencies are generally found to be "incoherent" owing to significant spatial-temporal variability of these waves within the ~11–18 km separations of the MMS spacecraft. The wave vectors of coherent LF whistler waves are oblique to the background magnetic field, with phase velocities along the normal in the shock NIF rest frame ranging from ~200–1,400 km/s (i.e., not phase standing). The wave vectors are typically oblique to the shock normal (median $\theta_{kn} = 54°$), with a preferential inclination toward the magnetic coplanarity plane (median angular departure of 41°). The rest frame frequencies of the LF whistler waves range from $f_{\circ} \sim 0.7 - 40$ Hz $= 0.04–6.3\ f_{\rm lh} = 1.7 - 270 f_{\rm ci}$ but are typically on the order of the lower-hybrid frequency (mean of 5.2 Hz $= 0.5 f_{\rm lh} = 21 f_{\rm ci}$). The wavelengths range from a few tens to a few hundred km (corresponding to $\lambda$ ~0.3–8.0 $\lambda_i$ or $\lambda$ ~13–343 $\lambda_e$). In the upstream half of the combined foot and ramp region, the scale distribution is dominated by whistlers at sub-ion inertial length scales ($\lambda$ ~0.65 ± 0.35$\lambda_i$). In contrast, ion scale whistlers dominate deeper in the layer yielding a double peaked scale distribution with peak enhancements at scales of $\lambda$ ~1.3 ± 0.6$\lambda_i$ and $\lambda$ ~4.0 ± 1.5$\lambda_i$, respectively.

The whistler associated Poynting fluxes are bursty in nature with intensities increasing with increasing penetration into the layer, with values ranging from a few hundredths to tenths of mW/m$^2$. The Poynting fluxes were primarily aligned quasiparallel to the shock surface, and antiparallel to the background magnetic field. In the foot, the Poynting fluxes were oriented within the coplanarity plane, while deeper in the ramp they were oriented preferentially in the out-of-coplanarity direction. The Poynting fluxes have a much smaller component along the shock normal, which, in the plasma rest frame, had a preferential upstream-directed sense across all resolved

spatial scales. However, in the shock NIF, a preferential downstream-directed sense across all resolved spatial scales was observed.

Energy exchange rates per unit volume $D_\circ$ were computed in the plasma rest frame in two frequency ranges for all four spacecraft. Values over the full range of frequencies (≤4,000 kHz) are typically on the order of a few hundredths of $\mu$W/m$^3$, with some examples reaching a few tenths of $\mu$W/m$^3$. Similar to the Poynting fluxes, the $D_\circ$ were bursty/patchy with values increasing with increasing penetration into the layer. The largest values of $D_\circ$ are associated with ES waves at 100 Hz to 8 kHz frequencies, with important contributions from signals at ∼30 Hz and below, which are attributed to the intense LF whistlers in the foot and into the ramp. Though the largest values of $D_\circ$ are associated with ES waves, the cumulative sums of $D_\circ$ through the layer indicate that the dominant net energy exchange contribution is from the LF whistler waves, with the HF ES waves providing negligible/net zero total contribution from individual packets in the interval. This latter behavior is owing to the symmetric oscillatory nature of the HF ES waves about the mean field in the interval.

Values for $D_\circ$ at frequencies ≤30 Hz are preferentially negative in the foot, while in the ramp region they are preferentially positive. In the former region, the dominant contributions are from the sub-ion inertial length whistler waves with important non-negligible contributions from ion inertial scale whistlers. These contributions yielded a net amount of energy exchanged from the plasma to the whistlers indicating that the foot is a source region of the LF whistlers. In the ramp region, the largest values for $D_\circ$ at frequencies ≤30 Hz are associated with whistler waves with ion inertial length scales, with exception at a few intermittent localized steps where large amplitude whistlers at sub-ion scales dominate. These contributions yield net energy dissipation from the waves to the plasma.

The Poynting flux and energy conversion rate spectral densities were found to have a similar qualitative power law dependence on scale. The spectral densities were found to increase with increasing scale (at and below the ion inertial length scale in the upstream half and at all scales deeper in the layer). The correlated data were used to quantify empirical scaling relationships, which provide important basis for comparison with theoretical models and simulations of energy transport and conversion at collisionless shocks.

Multi-spacecraft data comparisons revealed that the spatial and temporal properties of the LF whistler associated Poynting fluxes and energy conversion rates depend on location within the layer. This is exemplified by the cumulative sums of these quantities, which show little differences among the spacecraft measurements in the first half of the layer, while significant space-time variability is observed deeper in the ramp. The former indicates that whistler wave production and associated energy transport are coherent there. The latter is attributable to the reduced coherency of the whistler waves above ∼10 Hz in that region. This may be consequent to the spectrum of wave packets, unable to "group stand" against the flow, being blown back to the ramp, where they pile up and interfere with each other as they interact with the increasing magnetic field and density gradients. In some intermittent instances deeper in the ramp, the interaction process results in a localized spectrum of large amplitude whistler waves, which induce sharp localized changes or steps in net energy conversion and transport.

The results reported here (e.g., the characteristic spatial scales, and upstream-directed oblique wave vectors and plasma frame Poynting fluxes) are consistent with the MTSI-FD source mechanism of the LF whistler waves observed at the shock as suggested by Hull et al. (2020). These results combined with those of Hull et al. (2020) provide a more comprehensive understanding of the important role played by LF whistlers in energy reconfiguration at this high Mach number collisionless shock with ramifications to electron heating. The scenario suggested by these combined results is that LF whistler waves generated in the shock foot region (via the MTSI-FD) transport energy predominately along the shock surface and slightly toward the shock ramp in the shock normal incidence frame, where wave energy accumulates and is dissipated via Landau damping into electron heating.

## Appendix A: On the Direction of the Poynting Flux for LF Whistlers

Our model plasma in the foot is characterized by a double anisotropy: one defined by the direction of the background magnetic field $\mathbf{B_0}$, the other by the drift of the reflected ion beam $\mathbf{V_b}$. Let $\Psi = (\mathbf{B_0}, \mathbf{V_b})$ be the plane that is defined by these two directions. Theoretically, $\Psi$ contains the wave vectors of the most unstable whistlers destabilized by the reflected beam. Also, detailed measurements of the waves during the 04 November 2015

quasiperpendicular shock crossing show their vectors to lie close to the $\Psi$ plane (Hull et al., 2020, Section 3.5). Let us consider a whistler with a wave vector $\mathbf{k}$ in the plane $\Psi$, making an angle $\theta_{kb}$ with $\mathbf{B_0}$. We define an orthonormal coordinate system associated with the wave by ($L$, $T_1$, $T_2$) where $L$ is parallel to $\mathbf{k}$, $T_1$ is perpendicular to $\Psi$, and $T_2$ is within $\Psi$ and completes the system. See Figure A1.

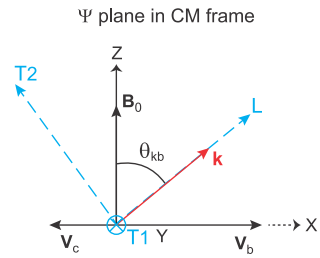


**Figure A1.** Illustration of the orientation of the wave vector $\mathbf{k}$, background magnetic field $\mathbf{B_0}$, and velocities of the incoming solar wind ion core $\mathbf{V_c}$ and reflected ion beam $\mathbf{V_b}$ in the $\Psi$ plane in the center of mass frame (This Figure was originally published in the work by Muschietti and Lembège (2017b) under the Creative Commons Attribution 3.0 License (https://creativecommons.org/licenses/by/3.0/)).

The Poynting vector reads

$$\mathbf{S} = \frac{1}{\mu_0} < \mathbf{E} \times \mathbf{B} >, \tag{A1}$$

where the averaging indicated by the brackets has to be done over some periodicity in the fields. In the coordinate system ($L$, $T_1$, $T_2$), and working in the center of mass frame, $\mathbf{S}$ has the following components

$$\begin{aligned} S_L &= \frac{1}{\mu_0} < E_{T1} B_{T2} - E_{T2} B_{T1} > \\ S_{T1} &= -\frac{1}{\mu_0} < E_L B_{T2} > \\ S_{T2} &= -\frac{1}{\mu_0} < E_L B_{T1} >. \end{aligned} \tag{A2}$$

The properties of beam-driven oblique whistlers were studied using pseudo-oblique full particle PIC simulations, where the propagation angle $\theta_{kb}$ is predetermined by the setup to one spatial direction (Muschietti & Lembège, 2016, 2017a). Due to the complex polarization of the wave, which includes a longitudinal component $E_L$, the Poynting vector is not parallel to $\mathbf{k}$. It was also shown that $< E_L B_{T2} >$ averages to zero whereas $< E_L B_{T1} >$ does not. In fact, for $\theta_{kb} < \pi/2$ the relative phases between $E_L$ and $B_{T1}$ are such that $< E_L B_{T1} >$ is negative, hence $S_{T2} > 0$. As a result, the Poynting vector also lies within $\Psi$ and makes an angle to $\mathbf{B_0}$ smaller than $\theta_{kb}$.

A convenient coordinate system for the plane $\Psi$ is to take $z$ along $\mathbf{B_0}$, $x$ along the part of the drift perpendicular to $\mathbf{B_0}$, and $y$ perpendicular to $\Psi$ unchanged from $T1$ (see Figure A1). In these coordinates $\mathbf{S}$ becomes

$$\begin{aligned} S_x &= S_L \sin\theta_{kb} - S_{T2} \cos\theta_{kb} \\ S_y &= S_{T1} \\ S_z &= S_L \cos\theta_{kb} + S_{T2} \sin\theta_{kb} \end{aligned} \tag{A3}$$

From simulations of whistler waves, one knows that the component $S_y$ averages to zero, $S_y = S_{T1} = 0$. So we are left with estimating which part is parallel ($S_z$) and perpendicular ($S_x$) to $\mathbf{B_0}$. If one further assumes that the direction of the Poynting vector parallels the group speed, the relative values of $S_{T2}$ and $S_L$ in Equation A3 can be evaluated as:

$$S_{T2}/S_L = -\frac{1}{k}\frac{\partial\omega}{\partial\theta_{kb}}\Big/\frac{\partial\omega}{\partial k}. \tag{A4}$$

In order to compute this ratio, we use the dispersion relation of LF whistler waves $\omega(k, \theta_{kb})$ in Muschietti and Lembège (2017b, Equation 1). In the limit $(kc/\omega_{\rm pe})^2 \ll 1$, we obtain

$$\begin{aligned} V_{gL} &= \frac{\partial\omega}{\partial k} = \frac{1+2\cos^2\theta_{kb}\,(k\lambda_i)^2}{\left(1+\cos^2\theta_{kb}\,(k\lambda_i)^2\right)^{1/2}}\mathrm{V_A} \\ V_{gT2} &= -\frac{1}{k}\frac{\partial\omega}{\partial\theta_{kb}} = \frac{\cos\theta_{kb}\,\sin\theta_{kb}\,(k\lambda_i)^2}{\left(1+\cos^2\theta_{kb}\,(k\lambda_i)^2\right)^{1/2}}\mathrm{V_A}, \end{aligned} \tag{A5}$$

where $\lambda_i \equiv c/\omega_{\rm pi}$ and $V_{\rm A}$ is the Alfvén velocity. Hence the ratio reads

$$\frac{S_{T2}}{S_L} = \frac{(k\lambda_i)^2\,\sin(2\,\theta_{kb})}{2+4(k\lambda_i)^2\cos^2\theta_{kb}} \tag{A6}$$

Thus, the parallel component $S_{\|}$ and the magnitude $S$ of the Poynting vector can be written in terms of $S_L$ as:

$$\begin{aligned} S\| = S_z &= \cos\theta_{kb}\left(1+\frac{(k\lambda_i)^2\sin^2\theta_{kb}}{1+2(k\lambda_i)^2\cos^2\theta_{kb}}\right)S_L \\ S &= \left[1+\frac{(k\lambda_i)^4\sin^2(2\,\theta_{kb})}{\left(2+4(k\lambda_i)^2\cos^2\theta_{kb}\right)^2}\right]^{1/2}S_L \end{aligned} \tag{A7}$$

This again shows the peculiar characteristic of oblique whistlers. Their group speed points closer to the background magnetic field $\mathbf{B_0}$ than the direction of their phase speed. To give a sense of the relative size of $S_{\|}$ to $S$, let us consider the 10 Hz whistler event that occurred 0805:35.397 UT listed in Table 2 of Hull et al. (2020), which is associated with $k\lambda_i = 11.6$ and an angle between $\mathbf{k}$ and $\mathbf{B_0}$ of $\theta_{kb} = 119°$. Using these values in Equation A7 one finds $S_{\|} = -1.26\ S_L$ and $S = 1.34\ S_L$. Therefore the angle of $\mathbf{S}$ versus $\mathbf{B_0}$ $\theta_{sb} = 161°$, which makes $\mathbf{S}$ more anti-parallel to $\mathbf{B_0}$ than the $\mathbf{k}$ vector. It is also in nice agreement with the data displayed in Figure 4i of the present paper.

In order to set the wave directions in the macro context, one should use GSE coordinates. Within these coordinates the plane $\Psi$ can have varied orientations due to the rotation of $\mathbf{B_0}$ and the change of $\mathbf{V_b}$ within the foot. The problem is intrinsically three-dimensional and needs be examined on a case by case basis. Figure A2 shows the relative orientations of various directions of interest determined at time 805:35.397 UT. At this foot location the plane $\Psi$ makes a 45° angle with the shock normal. As for the reflected beam velocity $\mathbf{V_b}$ (in red), it points 45.5° off the normal (in orange) and 15° off the motional electric field (in blue). Note that $\mathbf{V_b}$ is expected to parallel the normal close to the reflection point and to gyrate while accelerated by the motional electric field further upstream in the foot (e.g., Paschmann et al., 1982; Schwartz et al., 1983; Madanian et al., 2021, and references therein).

Our goal here is to assess the characteristic directions of the Poynting flux. Particularly, we wish to evaluate the sign of the Poynting flux along the shock normal and determine whether the wave energy is transported away from or toward the ramp. Recall that we work at this point in the center of mass frame (CM). Later on we will shift to the shock frame. Formally we can write

$$S_n = S_x\frac{\partial n}{\partial x} + S_z\frac{\partial n}{\partial z}, \tag{A8}$$

where $n$ is the unit vector in the shock normal direction.

Substituting $S_x$ and $S_z$ from Equation A3 one obtains after using Equation A6

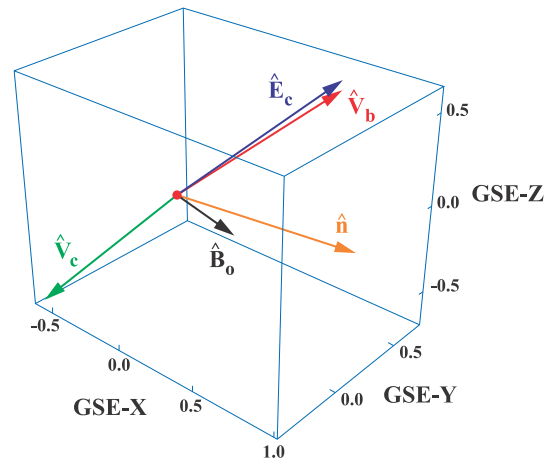


**Figure A2.** Three-dimensional illustration of unit vectors of interest in the center of mass frame (red dot) in GSE coordinates at time 0805:35.397 UT, which is in the first half of the layer. The background magnetic field $\hat{\mathbf{B}}_\mathbf{0}$ is indicated by solid black arrow, the incoming solar wind ion core velocity $\hat{\mathbf{V}}_\mathbf{c}$ by green arrow, the reflected ion beam velocity $\hat{\mathbf{V}}_\mathbf{b}$ by the red arrow, the motional electric field $\hat{\mathbf{E}}_\mathbf{c}$ by the blue arrow, and the shock normal $\hat{\mathbf{n}}$ by the orange arrow. The direction of the reflected beam velocity vector points 45.5° off of $\hat{\mathbf{n}}$ and 15° of $\hat{\mathbf{E}}_\mathbf{c}$.

$$S_n = \frac{S_L}{1 + 2(k\lambda_i)^2 \cos^2\theta_{kb}} \times \left\{ \frac{\partial n}{\partial x} \sin\theta_{kb} \left(1 + (k\lambda_i)^2 \cos^2\theta_{kb}\right) + \frac{\partial n}{\partial z} \cos\theta_{kb} \left[1 + (k\lambda_i)^2 \left(1 + \cos^2\theta_{kb}\right)\right] \right\}. \tag{A9}$$

For a reflected beam $\partial n/\partial x > 0$. So the first term in the second line is positive. The second term is also positive since for the situation where $\mathbf{B_0}$ points toward the shock the product $\partial n/\partial z \cos\theta_{kb} > 0$. Hence $S_n$ has the sign of $S_L$ which is clearly a positive quantity.

As a numerical example, we consider the situation depicted in Figure A2 together with values for the 805:35.397 UT event from Tables 1 and 2 of Hull et al. (2020). The angle between the beam velocity and the shock normal is 45.5°, hence $\partial n/\partial x = 0.701$. The angle between $\mathbf{B_0}$ and the shock normal is 95.7°, hence $\partial n/\partial z = -0.099$. Also, we use $k\lambda_i = 11.6$ and $\theta_{kb} = 119°$ to evaluate Equation A9. One obtains $S_n = +0.437\ S_L > 0$. Although smaller than $|S_\parallel| = 1.26\ S_L$, it is a positive value indicating an upstream direction.

So far, we have worked in the center of mass frame (CM). What happens to $S_n$ when seen in the shock frame? One way to assess the effect of the frame transformation is to evaluate the change in group velocity between the two frames. In the CM frame the group velocity of the wave along the normal can be computed from Equation A5 as

$$\frac{V_{gn}}{\mathrm{V_A}} = \frac{\partial n}{\partial x} \sin\theta_{kb} \sqrt{1 + (k\lambda_i)^2 (1 + \cos(2\theta_{kb}))/2} + \frac{\partial n}{\partial z} \cos\theta_{kb} \left[1 + (k\lambda_i)^2 (3 + \cos(2\theta_{kb}))/2\right] / \sqrt{1 + (k\lambda_i)^2 \cos^2\theta_{kb}}. \tag{A10}$$

Seen in the shock frame, the normal component of the group velocity is simply $V_{gn} + \mathbf{V_{CM}} \cdot \mathbf{n}$, where the CM frame moves with speed $\mathbf{V_{CM}}$ versus the shock frame. $\mathbf{V_{CM}} \cdot \mathbf{n}$ is a negative quantity and if its module is larger than $V_{gn}$, the normal component evaluated in the shock frame is negative and so is the normal component of the Poynting flux.

Using again values relevant to our event ($k\lambda_i = 11.6$, $\theta_{kb} = 119°$, $\partial n/\partial x = 0.701$, $\partial n/\partial z = -0.099$) one obtains $V_{gn} = +4.9\ V_\mathrm{A}$. Since the flow along the normal is on the order of $5 - 6 V_\mathrm{A}$, we can expect the normal component of the Poynting flux to be negative unlike in the CM frame. The whistler wave packets are slowly convected back toward the ramp at a speed on the order of the Alfvén speed. This provides them with a rather long "residency

time" to interact with the reflected ion beam. Packets that have larger wave numbers and faster group speeds may be close to group standing.

## Data Availability Statement

The MMS data used in this study are publicly available at the MMS Science Data Center website https://lasp.colorado.edu/mms/sdc/public/. OMNI upstream solar wind pressures are available from https://omniweb.gsfc.nasa.gov/. This work was performed using software based on the commercial Interactive Data Language (IDL) software package. Data were downloaded and processed using publicly available IDL based SPEDAS software (Angelopoulos et al., 2019) available at https://spedas.org and wavelet based software from C. Torrence and G. Compo available at http://atoc.colorado.edu/research/wavelets. Specifically, wavelet transforms, power spectral densities, and polarization spectra were computed using the SPEDAS wav_data.pro routine (a wrapper to the Torrence and Compo wavelet transform routine wavelet. pro that produces additional data quantities). Coherencies and phases were computed via the Torrence and Compo wave_coherency.pro procedure. Barycenter average quantities (e.g., magnetic and electric fields) and currents based on curlometer method were computed using the SPEDAS lingradest. pro routine. Lists of available cribs that are part of the SPEDAS library that provide examples on how to download and process MMS data are available at http://spedas.org/wiki/index.php?title=-Crib_sheets and http://spedas.org/wiki/index.php?title=MMS_cribs. Key high-level data and a crib with some plotting examples are available at the Figshare link https://doi.org/10.6084/m9.figshare.24993429 (Hull et al., 2024).

**Acknowledgments**
Funding for the work by AJH and LM was provided by NASA Grant 80NSSC17K0609. AJH also acknowledges support from NASA Grant 80NSSC22K0521 and NSF Grant 1914670. The work of OVA was supported by NASA grants 80NSSC20K0697, 80NSSC22K0433, 80NNSC19K0848, 80NSSC20K0218, and 80NSSC22K0522. French involvement (SCM instruments) on MMS is supported by CNES and CNRS. We thank the MMS instrument teams and the MMS Science Data Center for providing the data.

## References

Angelopoulos, V., Cruce, P., Drozdov, A., Grimes, E. W., Hatzigeorgiu, N., King, D. A., et al. (2019). The space physics environment data analysis system (SPEDAS). *Space Science Reviews*, *215*(9), 1–46. https://doi.org/10.1007/s11214-018-0576-4

Bale, S. D., Balikhin, M. A., Horbury, T. S., Krasnoselskikh, V. V., Kucharek, H., Möbius, E., et al. (2005). Quasi-perpendicular shock structure and processes. *Space Science Reviews*, *118*(1–4), 161–203. https://doi.org/10.1007/s11214-005-3827-0

Balikhin, M. A., de Wit, T. D., Alleyne, H. S. C. K., Woolliscroft, L. J. C., Walker, S. N., Krasnosel'skikh, V., et al. (1997). Experimental determination of the dispersion of waves observed upstream of a quasi-perpendicular shock. *Geophysical Research Letters*, *24*(7), 787–790. https://doi.org/10.1029/97GL00671

Chanteur, G. (1998). Spatial interpolation for four spacecraft: Theory. In G. Paschmann & P. W. Daly (Eds.), *Analysis methods for multi-spacecraft data* (pp. 349–369). Eur. Space Agency.

Dimmock, A. P., Balikhin, M. A., Walker, S. N., & Pope, S. A. (2013). Dispersion of low frequency plasma waves upstream of the quasi-perpendicular terrestrial bow shock. *Annales Geophysicae*, *31*(8), 1387–1395. https://doi.org/10.5194/angeo-31-1387-2013

Dunlop, M. W., Southwood, D. J., Glassmeier, K.-H., & Neubauer, F. M. (1988). Analysis of multipoint magnetometer data. *Advances in Space Research*, *8*(9–10), 273–277. https://doi.org/10.1016/0273-1177(88)90141-X

Ergun, R. E., Tucker, S., Westfall, J., Goodrich, K. A., Malaspina, D. M., Summers, D., et al. (2016). The axial double probe and fields signal processing for the MMS mission. *Space Science Reviews*, *199*(1), 167–188. https://doi.org/10.1007/s11214-014-0115-x

Eriksson, A. (1998). Spectral analysis. In G. Paschmann & P. W. Daly (Eds.), *Analysis methods for multi-spacecraft data* (pp. 5–42). Eur. Space Agency.

Harvey, C. C. (1998). Spatial gradients and the volumetric tensor. In G. Paschmann & P. W. Daly (Eds.), *Analysis methods for multi-spacecraft data* (pp. 307–322). Eur. Space Agency.

Hull, A., Muschietti, L., Agapitov, O., Chaston, C., Le Contel, O., & Lindqvist, P.-A. (2024). Poynting flux and energy conversion rate data derived from MMS measurements at Earth's bow shock [Dataset]. *Figshare*. https://doi.org/10.6084/m9.figshare.24993429

Hull, A. J., Muschietti, L., Contel, O. L., Dorelli, J. C., & Lindqvist, P.-A. (2020). MMS observations of intense whistler waves within Earth's supercritical bow shock: Source mechanism, and impact on shock structure and plasma transport. *Journal of Geophysical Research: Space Physics*, *125*(7), e2019JA027290. https://doi.org/10.1029/2019JA027290

Hull, A. J., Muschietti, L., Oka, M., Larson, D. E., Mozer, F. S., Chaston, C. C., et al. (2012). Multiscale whistler waves within Earth's perpendicular bow shock. *Journal of Geophysical Research*, *117*(A12), 12104. https://doi.org/10.1029/2012JA017870

Krasnoselskikh, V., Balikhin, M., Walker, S. N., Schwartz, S., Sundkvist, D., Lobzin, V., et al. (2013). The dynamic quasiperpendicular shock: Cluster discoveries. *Space Science Reviews*, *178*(2–4), 535–598. https://doi.org/10.1007/s11214-013-9972-y

Krasnosel'skikh, V., Balikhin, M. A., Alleyne, H. S. C., Klimov, S. I., Mierjedrzejowicz, W. A. C., Pardaens, A. K., et al. (1991). On the nature of low frequency turbulence in the foot of strong quasi-perpendicular shocks. *Advances in Space Research*, *11*(9), 15–18. https://doi.org/10.1016/0273-1177(91)90002-2

Labelle, J., & Kintner, P. M. (1989). The measurement of wavelength in space plasmas. *Reviews of Geophysics*, *27*(4), 495–518. https://doi.org/10.1029/RG027i004p00495

Lalti, A., Khotyaintsev, Y. V., Graham, D. B., Vaivads, A., Steinvall, K., & Russell, C. T. (2022). Whistler waves in the foot of quasi-perpendicular supercritical shocks. *Journal of Geophysical Research: Space Physics*, *127*(5), e2021JA029969. https://doi.org/10.1029/2021JA029969

Le Contel, O., Leroy, P., Roux, A., Coillot, C., Alison, D., Bouabdellah, A., et al. (2016). The search-coil magnetometer for MMS. *Space Science Reviews*, *199*(1), 257–282. https://doi.org/10.1007/s11214-014-0096-9

LeDoc, M. J. (1998). *The wave normal and Poynting flux of magnetospheric plasma waves (Unpublished doctoral dissertation)*. University of Iowa. Ph. D. thesis.

Lindqvist, P.-A., Olsson, G., Torbert, R. B., King, B., Granoff, M., Rau, D., et al. (2016). The spin-plane double probe electric field instrument for MMS. *Space Science Reviews*, *199*(1), 137–165. https://doi.org/10.1007/s11214-014-0116-9

Lobzin, V. V., Krasnoselkikh, V. V., Bosqued, J.-M., Pincon, J.-L., Schwartz, S. J., & Dunlop, M. (2007). Nonstationarity and reformation of high-Mach-number quasiperpendicular shocks: Cluster observations. *Geophysical Research Letters*, *34*(5), L05107. https://doi.org/10.1029/2006GL029095

Madanian, H., Desai, M. I., Schwartz, S. J., Wilson, L. B., III, Fuselier, S. A., Burch, J. L., et al. (2021). The dynamics of a high mach number quasi-perpendicular shock: MMS observations. *The Astrophysical Journal*, *908*(40), 40. https://doi.org/10.3847/1538-4357/abcb88

Matsukiyo, S., & Scholer, M. (2006). On microinstabilities in the foot of high Mach number perpendicular shocks. *Journal of Geophysical Research*, *111*(A6), A06104. https://doi.org/10.1029/2005JA011409

Muschietti, L., & Lembège, B. (2016). Two types of whistler instabilities in the foot of quasi-perpendicular supercritical shocks: A poynting flux analysis. *Presented at American Geophysical Union fall meeting* (p. SH21A-2505). San Francisco.

Muschietti, L., & Lembège, B. (2017a). Identification of two types of whistler instabilities excited in the foot of quasi-perpendicular supercritical shocks: A poynting flux analysis. *Presented at European. Geosciences Union general assembly* (p. EGU2017-8780).

Muschietti, L., & Lembège, B. (2017b). Two-stream instabilities from the lower-hybrid frequency to the electron cyclotron frequency: Application to the front of quasi-perpendicular shocks. *Annales Geophysicae*, *35*(5), 1093–1112. https://doi.org/10.5194/angeo-35-1093-2017

Paschmann, G., Sckopke, N., Bame, S. J., & Gosling, J. T. (1982). Observations of gyrating ions in the foot of the nearly perpendicular bow shock. *Geophysical Research Letters*, *9*, 881–884.

Pollock, C., Moore, T., Jacques, A., Burch, J., Gliese, U., Saito, Y., et al. (2016). Fast plasma investigation for magnetospheric multiscale. *Space Science Reviews*, *199*(1), 331–406. https://doi.org/10.1007/s11214-016-0245-4

Russell, C. T., Anderson, B. J., Baumjohann, W., Bromund, K. R., Dearborn, D., Fischer, D., et al. (2016). The magnetospheric multiscale magnetometers. *Space Science Reviews*, *199*(1), 189–256. https://doi.org/10.1007/s11214-014-0057-3

Schwartz, S. J., Thomsen, M. F., & Gosling, J. T. (1983). Ions upstream of the Earth's bow shock: A theoretical comparison of alternative source populations. *Journal of Geophysical Research*, *88*(A3), 2039–2047. https://doi.org/10.1029/JA088iA03p02039

Sundkvist, D., Krasnoselskikh, V., Bale, S. D., Schwartz, S. J., Soucek, J., & Mozer, F. (2012). Dispersive nature of high mach number collisionless plasma shocks: Poynting flux of oblique whistler waves. *Physical Review Letters*, *108*(2), 025002. https://doi.org/10.1103/PhysRevLett.108.025002

Swanson, D. G. (1989). *Plasma waves*. Academic Press Inc.

Torrence, C., & Compo, G. P. (1998). A practical guide to wavelet analysis. *Bulletin America Meteorology Social*, *79*(1), 61–78. https://doi.org/10.1175/1520-0477(1998)079<0061:APGTWA>2.0.CO;2

Torrence, C., & Webster, P. J. (1999). Interdecadal changes in the ENSO-monsoon system. *Journal of Climate*, *12*(8), 2679–2690. https://doi.org/10.1175/1520-0442(1999)012⟨2679:ICITEM⟩2.0.CO;2

Wilson, L. B., III. (2016). Low frequency waves at and upstream of collisionless shocks. In A. Keiling, D.-H. Lee, & V. Nakariakov (Eds.), *Low-frequency waves in space plasmas low-frequency waves in space plasmas* (Vol. 216, pp. 269–291). AGU. https://doi.org/10.1002/9781119055006.ch16

Wilson, L. B., III, Sibeck, D. G., Breneman, A. W., Contel, O. L., Cully, C., Turner, D. L., et al. (2014a). Quantified energy dissipation rates in the terrestrial bow shock: 1. Analysis techniques and methodology. *Journal of Geophysical Research: Space Physics*, *119*(8), 6455–6474. https://doi.org/10.1002/2014JA019929

Wilson, L. B., III, Sibeck, D. G., Breneman, A. W., Contel, O. L., Cully, C., Turner, D. L., et al. (2014b). Quantified energy dissipation rates in the terrestrial bow shock: 2. Waves and dissipation. *Journal of Geophysical Research: Space Physics*, *119*(8), 6475–6495. https://doi.org/10.1002/2014JA019930

Wu, C. S., Zhou, Y. M., Tsai, S. T., Guo, S. C., Winske, D., & Papadopoulos, K. (1983). A kinetic cross-field streaming instability. *Physics of Fluids*, *26*(5), 1259–1267. https://doi.org/10.1063/1.864285